



## Effect of powder-pack aluminizing on microstructure and oxidation resistance of wire arc additively manufactured stainless steels

Uğur Gürol<sup>a</sup>, Yasemin Altınay<sup>b</sup>, Ali Günen<sup>c,\*</sup>, Ömer Saltuk Bölükbaşı<sup>c</sup>, Mustafa Koçak<sup>d</sup>, Gürel Çam<sup>e</sup>

<sup>a</sup> Istanbul Gedik University, Faculty of Engineering, Department of Metallurgical & Materials Engineering, Istanbul, Türkiye

<sup>b</sup> Mustafa Kemal Üniversitesi, Teknoloji ve Ar-Ge Uygulama ve Araştırma Merkezi (MARGEM), Hatay, Türkiye

<sup>c</sup> Iskenderun Technical University, Faculty of Engineering and Natural Sciences, Department of Metallurgy and Materials Engineering, 31200 Iskenderun, Hatay, Türkiye

<sup>d</sup> Istanbul Gedik University, Faculty of Engineering, Dept. of Mechanical Engineering, Istanbul, Turkey

<sup>e</sup> Iskenderun Technical University, Faculty of Engineering and Natural Sciences, Department of Mechanical Engineering, 31200 Iskenderun, Hatay, Türkiye

### ARTICLE INFO

#### Keywords:

Wire arc additive manufacturing  
Stainless steel  
Aluminizing  
Characterization  
Oxidation resistance

### ABSTRACT

This study investigated the effect of powder-pack aluminizing treatment on the high-temperature oxidation of ER307 stainless steel components fabricated by wire arc additive manufacturing (WAAM) during isothermal oxidation at 1000 °C for 5 h, 25 h, and 50 h. Scanning electron microscopy (SEM), energy dispersion spectroscopy (EDS), X-ray diffraction (XRD), X-Ray fluorescence (XRF), nanoindentation testing, and oxidation testing were used to characterize the aluminized and non-aluminized samples produced by WAAM. The results showed that the powder-pack aluminizing increased the surface nano-hardness up to 13.95 GPa and the modulus of elasticity up to 159 GPa, as well as improving the microstructure of WAAM ER307 stainless steel. Indeed, aluminide coatings remained stable up to temperatures exceeding 1000 °C, and the growth of hematite, the main oxide phase, was inhibited by a preferential alumina growth (Al<sub>2</sub>O<sub>3</sub>), resulting in an improvement in oxidation resistance in the range of 46–70 %. In addition, owing to the advantages of low-temperature aluminizing, the microstructure, mechanical properties, and oxidation resistance of these alloys have been improved without causing sigma phase formations, which constitute a significant problem in high-temperature heat treatment of stainless steels.

### 1. Introduction

Stainless steels, which started to be produced at the beginning of the 20th century, are ferrous alloys containing at least 10.5 % chromium (Cr) in their composition [1–3]. In addition, other alloying elements such as nickel (Ni), molybdenum (Mo), manganese (Mn), titanium (Ti), nitrogen (N), and aluminum (Al) have been added in addition to Cr over time to make stainless steels more resistant to tribo-corrosive environments. As a result, it is known that there are >150 stainless steel grades today [3–5].

Until the 2000s, stainless steels were first produced by casting or powder metallurgy methods; then, it was turned into the final product by secondary processes such as forging, subtractive processes (i.e., machining), and heat treatment, etc. [3]. Casting and powder metallurgy methods have advantages over each other. Although the casting method is an advantageous production process for mass production,

solidification in the casting process often results in segregation [6,7]. This adversely affects the mechanical properties and corrosion resistance. On the other hand, powder metallurgy can effectively eliminate the solidification segregation of stainless steel, allowing for increases in alloy levels to further improve the overall mechanical properties. However, the high cost of powders, the necessity of mechanical alloying of powders, and multiple production processes such as pressing, sintering, and material inspection, as well as the size and complex geometry restrictions are the limitations of this method compared to the casting method [8,9]. In forging and machining, on the other hand, multiple production processes, such as removing chips or descaling (removal of the surface oxides), which are necessary for giving the final shape, prevent these alloys from being produced cost-effectively [10]. In addition, the necessity of model and mold preparation in the production by casting and forging cause these methods to be costly for producing final components.

\* Corresponding author.

E-mail address: [ali.gunen@iste.edu.tr](mailto:ali.gunen@iste.edu.tr) (A. Günen).

<https://doi.org/10.1016/j.surfcoat.2023.129742>

Received 10 May 2023; Received in revised form 14 June 2023; Accepted 20 June 2023

Available online 22 June 2023

0257-8972/© 2023 Elsevier B.V. All rights reserved.

In recent years, these limitations in traditional stainless steel production processes have led scientists and the industrial environment to work on the manufacturability of stainless steel through additive manufacturing. The 3D metal production studies, the trials of which started in 1991 [11], ensure the industrial production of stainless steels by the additive manufacturing method with the application of the direct laser sintering machine of the German EOS company towards the 2000s [12].

After the 3D model designed by a computer-aided design (CAD) software is decomposed into 2D layers with special software, afterwards, it is transferred to 3D printer to be fabricated layer by layer according the CAD design. Complex metallic parts that are difficult to manufacture by conventional production methods can be efficiently designed and produced quickly with additive manufacturing [13,14]. However, as with casting, forging, and powder metallurgy methods, the additive manufacturing method also has its limitations. The most important of these are the microstructural heterogeneities observed in the parts produced and the difficulty of reproducibility of the same mechanical properties [15]. It has been reported in many studies that polymeric materials, aluminum alloys, steels, superalloys, and ceramic matrix composites have been produced by additive manufacturing methods in recent years [16–20]. Due to their use in advanced engineering applications such as aviation, space, nuclear, medical, and heat treatment equipment, stainless steels are among the alloys most produced by the additive manufacturing method [21,22].

There are currently seven additive manufacturing processes as defined in ASTM F2792-12A Standard. The fact that the arc power of the directed energy deposition-arc (arc-DED), also known as wire arc additive manufacturing (WAAM) process, is 5–10 times time-efficient (i.e., DED-GMA) than those of powder bed fusion (PBF-LB) and directed energy deposition using laser beam (DED-LB) methods [23–25] makes it more cost-effective to manufacture stainless steels products [26]. However, stainless steel's low thermal conductivity and high thermal expansion make these alloys more susceptible to elemental segregation and solidification cracking during WAAM production [21].

Stainless steel types are frequently preferred in industrial applications due to the thin but dense chromium oxide layer ( $\text{Cr}_2\text{O}_3$ ) formed by the chromium element on the surface, providing high oxidation resistance in acidic environments and atmospheric conditions and having a bright surface appearance [1,3,4]. Their corrosion resistance at high temperatures is due to the protective oxides they form on the surface, such as  $\text{NiO}$ ,  $\text{Cr}_2\text{O}_3$ , and  $\text{NiCr}_2\text{O}_4$  [27]. Stainless steels are generally used in cutting tools, manufacturing of kitchen sinks, chemical storage tanks, hot water storage units, exterior cladding, kitchen utensils, surgical materials, car chassis components, seamless pipes, tubes, and at room temperature conditions such as food storage tanks [28–33]. However, except for some types of stainless steels (e.g., some ferritic stainless steels), the  $\text{Cr}_2\text{O}_3$  layer on the other stainless steels, which provides satisfactory protection against many environments at room conditions, causes degradation as it loses its resistance to scaling at  $\sim 600\text{--}650\text{ }^\circ\text{C}$  [34].

Alloying or surface modifications (boriding, titanizing, aluminizing, etc.) are used to improve the resistance of stainless steels, which are used in high-temperature applications due to their cost-effectiveness in harsh tribocorrosive environments [35,36]. Protective coatings are one of the main approaches within the scope of surface modifications. It is possible to improve the surface properties more cost-effectively by surface treatments and/or coating techniques without changing the chemical composition of the entire material [37–39]. The primary purpose of these processes is to improve the surface's mechanical properties and corrosion properties without causing a change in the material's microstructure. Thus, the service life and functional efficiency are extended without changing the material's internal structure. Especially in applications where high-temperature oxidation resistance is desired, aluminide coatings are applied effectively in the literature [40–42]. Because the Al in the content of aluminide coatings has a high affinity for oxygen,

thus forms an  $\text{Al}_2\text{O}_3$  layer on the surface which acts as a barrier for oxidation to penetrate the interior. Many publications in the open literature are on improving high-temperature oxidation resistance by pack aluminizing of stainless steel produced by casting and powder metallurgy methods [40–44]. On the other hand, it has been determined that aluminizing studies on stainless steels produced with different additive manufacturing methods since the 2000s have not yet been introduced to the literature. Therefore, their effects have yet to be discussed.

Therefore, considering the oxidation problem of stainless steels in harsh conditions (above  $650\text{ }^\circ\text{C}$ ) where high oxidation resistance is required, such as nuclear, coal, and biomass power plants [21,22], this study focuses on the use of aluminide coating for the improvement of oxidation resistance of stainless steels (e.g., AISI 307) parts fabricated by the WAAM techniques, which are increasingly used. The obtained coatings were characterized by SEM, EDS, XRD, and nanoindentation and compared with untreated as-built ER307 stainless steel by exposure to open air for 5 h, 25 h, and 50 h at  $1000\text{ }^\circ\text{C}$ . Therefore, this study has the potential to be an important reference for academic studies and industrial applications of oxidation-resistant stainless steel with surface aluminizing for additively manufactured components.

## 2. Materials and method

### 2.1. Production of WAAM ER307 stainless steel component

In producing ER307 stainless steel components, the WAAM method was used, which allows the production of complex-shaped and larger metallic components at lower costs compared to other additive manufacturing methods [17,26]. 1.2 mm diameter ER307 (acc. to AWS A5.9) solid wire was used to produce WAAM samples having a dimension of  $350 \times 75 \times 12$  mm deposited on an AISI 304 stainless steel substrate. The chemical composition of the wire for WAAM method (modified ER307) was determined by XRF analysis as 17.05Cr, 8.95 Ni, 6.18 Mn, 0.56 Si, 0.31 Cu, 0.05 C, 0.03 Mo, 0.019 P, 0.017 S (in wt%) and balance Fe. The component was produced by a GeKa-Tec WB 500 L welding machine with a water-cooled torch integrated into a 6-axis OTC Daihen D-V8L robot. The single passes were deposited by stringer mode on the previous layer to obtain the final component. A dwell time of 120 s is employed to help the component transfer excessive heat to the environment. In addition, the pass direction was reversed each time to avoid build-up at the start and end of the paths. The following specifications were employed to build the component: an arc voltage of 14.7 V, an arc current of 120 A, a scan rate of 50 cm/m, and a shielding gas mixture of 97.5 % Ar and 2.5 %  $\text{CO}_2$  with a flow rate of 15 L/min.

The chemical composition of ER307 stainless steel produced with the parameters mentioned above was determined by XRF analysis as 16.97 Cr, 8.11 Ni, 4.96 Mn, 0.58 Si, 0.20 Cu, 0.04C, 0.03 Mo, 0.023 P, 0.017 S (in wt%) and balance Fe. Since surface roughness ( $R_a$ ) of an average of  $62.5\text{ }\mu\text{m}$  is relatively high for the coating process in the production parts with WAAM, the samples were machined with a CNC machine after production to obtain a surface roughness of  $<1\text{ }\mu\text{m}$ . Then, the surface was ground with 1000 SiC sandpaper to remove the residues on the surface. After these surface preparation processes, the samples were cut in dimensions of  $20 \times 20 \times 5$  mm for the coating processes and oxidation tests.

### 2.2. Powder-pack aluminizing

Based on the investigations existing in the open literature, it was decided that the best powders for the aluminizing process were 30 % pure metallic Al powder ( $25\text{ }\mu\text{m}$ ), which supplies aluminum, 10 %  $\text{NH}_4\text{Cl}$  ( $25\text{ }\mu\text{m}$ ), which forms chloride gas, and 60 %  $\text{Al}_2\text{O}_3$  ( $25\text{ }\mu\text{m}$ ), which inhibits oxidation and prevents sintering [42]. During the pack aluminizing process, the cleaned sample surfaces were placed in the center of crucibles made of Inconel 718 Ni-based superalloys. The samples to be

coated were placed inside the container in a way that ensures a minimum of 10 mm of aluminizing powder covers all sides of the samples, and the containers with threaded mouths were tightly sealed to prevent air ingress. The studies in the literature were examined to select the aluminizing conditions. An aluminizing process at 700 °C for 3 h was chosen with the assumption that an aluminide coating layer of around 40 µm could be obtained [40–42]. Aluminizing processes were carried out in a controlled atmosphere furnace environment due to its cost-effectiveness in industrial applications. The samples were taken from the furnace after aluminizing and left to cool in an open-air environment.

### 2.3. Microstructural characterization and oxidation tests

After powder-pack aluminizing, the samples' cross-sections were examined following the usual mechanical grinding and polishing processes. Since the aluminide coatings could be observed clearly under scanning electron microscopy (SEM) in the as-polished condition, no etching was required. The samples' cross-sectional views were examined using a Thermo Fisher Scientific Apreo S LoVac SEM apparatus. Circular Backscatter (CBS) detector, 15 kV accelerating voltage, and 11 mm spot size was used in SEM investigations, and EDS analyses to more precisely characterize the morphology, microstructure, and chemical composition. With a Hysitron TI-950 TriboIndenter device, nanoindentation tests were performed utilizing a Berkovich-tip nanoindentation with a 10 mN load, 30 s continuous loading rate, 15 s dwell time, and 30 s gradual unloading period [45,46]. A computer-controlled analytical empyrean apparatus was used to determine the phases present in the aluminide layers obtained by the aluminizing process and the oxide layers that formed on the surface following oxidation. Cu K<sub>α</sub> radiation (1.5418 Å) with a scan step size of 0.0525211 and 2 angles ranging from 10 to 90° were identified as the XRD parameters.

Isothermal oxidation tests were performed at 1000 °C, considering the maximum temperature that stainless steel may encounter in high-temperature applications in nuclear, coal, and biomass power plants [29,33–35]. The oxidation time was determined as 5, 25, and 50 h and oxidation tests were performed in an open-air environment in an electric oven (Protherm PLF 130/12), Turkey). Oxidation tests were performed on samples with an equal surface area of 15 × 15 × 5 mm<sup>3</sup>. The samples were weighed in alumina crucibles before and after the oxidation test with a precision of 1 × 10<sup>-4</sup> g, and the weight gains were determined in this way. Similarly, the average oxide layer thickness of each oxidized sample was determined by taking 5 measurements from each of the five different SEM images. Three samples from each sample were exposed to an oxidation test, and their averages were used to calculate oxidation weight gains. The oxide layers formed on the surface of the samples

exposed to the oxidation test were examined by XRD and SEM, and EDS. In addition, the oxidation mechanisms formed on the surface were investigated.

## 3. Results and discussions

### 3.1. Microstructure of As-built WAAM ER307

Figs. 1a and b show the microstructures of the middle region of the component manufactured with WAAM. The microstructural examinations indicated that the interface between layers was well bonded without macro-sized pores and solidification cracks. As a result, good metallurgical bonding was achieved. The white regions are austenite, while the dark regions confirm the existence of δ-ferrites. The amount of residual ferrite was measured using a ferrite scope and results were found as about 3.2 ± 0.1 % in the middle of the WAAM component whereas the root and top were 3.5 ± 0.2 and 3.5 ± 0.1 %, respectively.

The top of the interface corresponding to the non-melted region mainly comprises a fine columnar structure with an acicular shape of δ-ferrites perpendicular to the deposition direction in an austenitic (γ) matrix. Since the remelted zone is the first area of the volume to solidify, the higher cooling rates there may account for this [47]. In contrast, the bottom part of the interface exhibits a decreased amount of δ-ferrite having globular, skeletal, and lathy morphologies due to lower cooling rates than the top section. The microhardness values in the middle of the WAAM 307 component varied between 168 and 179 HV, and the average along the building direction was 173 ± 3 HV. The highest hardness values through any of the layers were measured at remelted regions of the layers (top of the interface) where the higher amounts of δ-ferrites with small grain sizes existed.

### 3.2. Characterization of aluminide layer

The SEM micrograph of the coating layer formed on the sample surface exposed to the aluminizing process at 700 °C for 3 h and the result of EDS line analysis are presented in Fig. 2.

Fig. 2 shows that the cross-sectional microstructure of WAAM ER307 stainless steel component exposed to aluminizing consists of a 43 ± 2.5 µm thick single-layer coating layer and a 2.5–3.5 µm thick transition zone between the coating layer and the matrix. This transition zone between the coating layer and the substrate allows the coatings to bond to the matrix with a high adhesion force [48,49]. When the result of EDS line analysis is examined, although the coating layer consists of Al, Fe, Cr, and Ni, the atomic ratios of these elements are in the range of 60–65 %, 20–25 %, 5–6 %, and 0–5 %, respectively, and are close to stable. This indicates that the aluminizing time is sufficient. Because if the

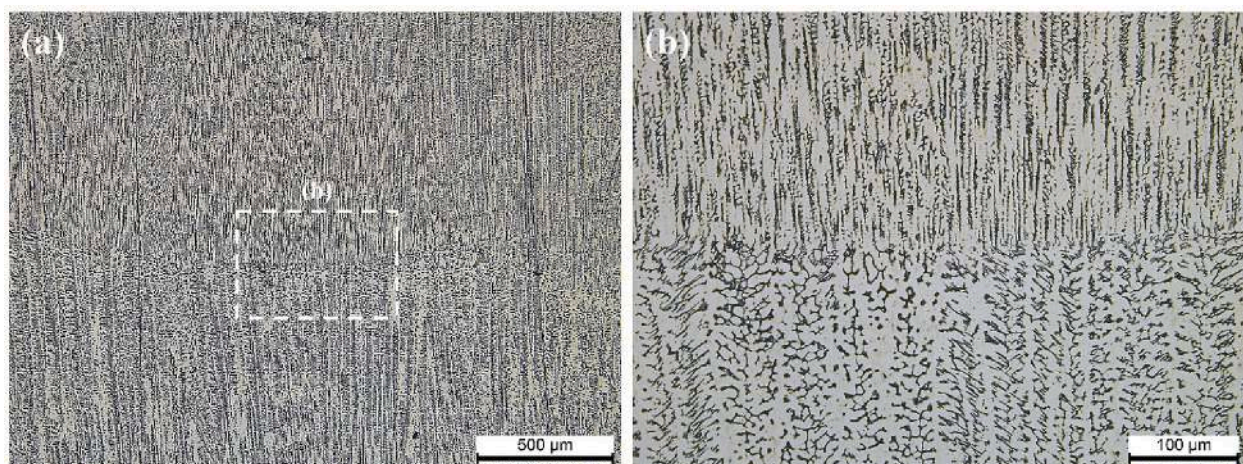


Fig. 1. Optical micrographs of the middle region of the ER307 stainless steel component fabricated by WAAM at different magnifications: a) 20× and b) 100×.

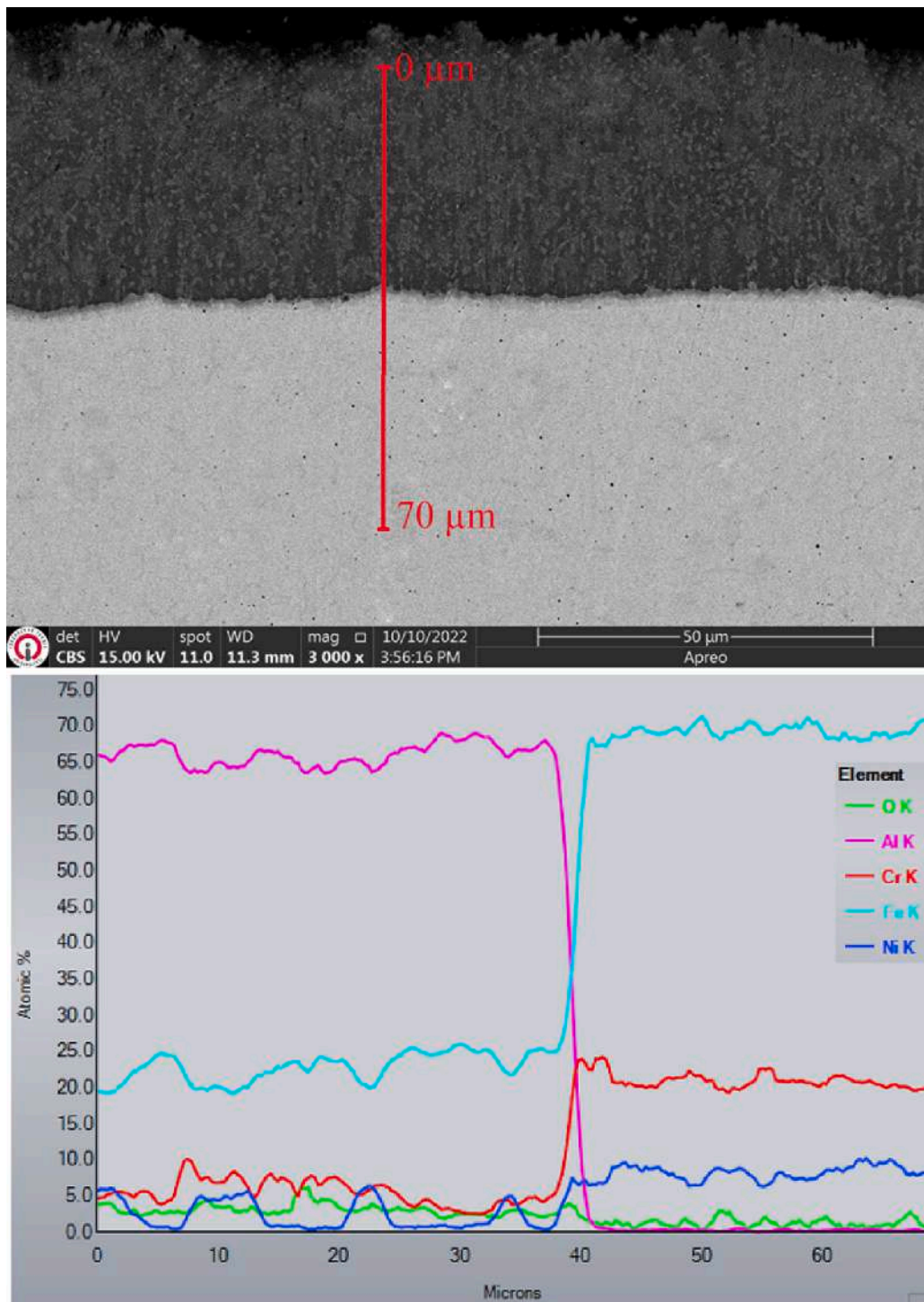


Fig. 2. Cross-sectional SEM micrograph of the aluminide coating layer formed on the surface of the WAAM ER307 stainless steel alloy and the result of EDS line analysis.

processing time were short in pack aluminizing processes, it would be expected that the aluminum ratio would decrease from the outer surface to the inner part [42,50,51]. As indicated in the literature, Li et al. [52] obtained a coating layer consisting of FeAl and  $\text{Fe}_3\text{Al}$  with a thickness of 80  $\mu\text{m}$  on the surface of AISI 321 steel after aluminizing at 950  $^\circ\text{C}$  for 12 h. Studies in the literature show that the tensile strength and elongation of the steel do not change with the variation of coating layer thickness in cases where the coating thickness obtained on stainless steel is <150  $\mu\text{m}$ . However, the mechanical properties decrease with the layer thickness increase in cases where the aluminide layer thickness is >200  $\mu\text{m}$

[52–54]. This phenomenon was expected regarding  $\text{Cr}_{23}\text{C}_6$  precipitation in the microstructure due to the high temperature and long processing times, and sigma phase formation rather than the coating thickness. Many scholars have studied low-temperature aluminizing to overcome these limitations [42,55–57]. The coating thicknesses obtained in this study agreed with the studies on low-temperature aluminizing in the literature [43,44,55,56].

Fig. 3 shows the XRD patterns of untreated as-built WAAM ER307 stainless steel samples and aluminide-coated samples at 700  $^\circ\text{C}$  for 3 h. When Fig. 3 is examined, the untreated as-built WAAM ER307 specimen

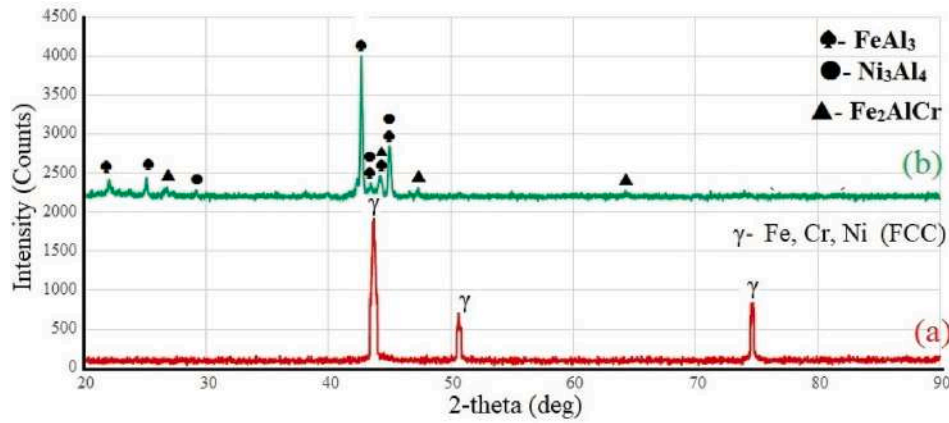


Fig. 3. XRD patterns taken from the surface of WAAM ER307 alloy: a) as-built specimen and b) specimen exposed to aluminizing at 700 °C for 3 h.

consists of  $\gamma$ -austenite phase (FCC) with sharp peaks in the (111), (200), and (220) planes (JCPDS card number: 00–035-1375). As seen in Fig. 3a), only strong diffraction peaks of  $\gamma$ -austenite were observed in the XRD pattern of the as-built WAAM ER307 stainless steel while  $\delta$ -ferrites were not observed. In previous studies in the literature, it was stated that delta-ferrite was not observed in XRD analysis, it was measured by the ferritoscope in the as-built structure, and  $\delta$ -ferrites were almost 3.5–4.2 % in the microstructure [58,59].

On the other hand, in the aluminide layer, in addition to the dominant phase  $\text{FeAl}_3$ , there are minor phases  $\text{Ni}_3\text{Al}_4$  and  $\text{Fe}_2\text{AlCr}$  in the structure. Considering the Fe–Al binary phase diagram published by Murray 1992 given in Fig. 4, it is seen that the Al concentration of the  $\text{FeAl}_3$  phase is approximately 58–61 % [60]. Compared to the SEM-EDS line analysis results shown in Fig. 2, the Al concentration at 35  $\mu\text{m}$  depth was found to be ~60 % by atomic weight. Therefore, the XRD results obtained showed excellent agreement with the results from the SEM-EDS line analysis shown in Fig. 2.

Studies show that different phase formations may occur depending on variation of aluminizing temperature and time [40–42,50–57]. The

general opinion in the literature is that only the  $\text{Fe}_2\text{Al}_5$  phase will form in short aluminizing times, and as time increases, the phase structure will turn into the  $\text{FeAl}_3$  phase [57,61]. For instance, Sun et al. reported that the possible order of formation of the iron-aluminum compounds in the aluminizing process is  $\text{Fe}_2\text{Al}_5 > \text{FeAl}_3 > \text{FeAl}_2 > \text{FeAl}$ , and the  $\text{Fe}_3\text{Al}$  phase does not form when the temperature is higher than 400 °C because its free energy is greater than zero [55]. In addition, the fact that the Fe-aluminide phases (i.e.,  $\text{FeAl}$ ,  $\text{FeAl}_2$ ,  $\text{FeAl}_3$ , and  $\text{Fe}_2\text{Al}_5$ ), which may occur in the Fe–Al diagram shown in Fig. 4, maintain their stability up to temperatures up to 1100 °C, indicates that the aluminide phases formed on the surface of the as-built WAAM ER307 specimen act as protector for the substrate material against high-temperature damages.

### 3.3. Nano-hardness and modulus of elasticity

By conducting the aluminizing treatment at 700 °C for 3 h, a spheroidization heat treatment was also applied to the ER307 stainless steel component fabricated with WAAM at the same time. In addition, nanoindentation tests were performed to determine the effect of

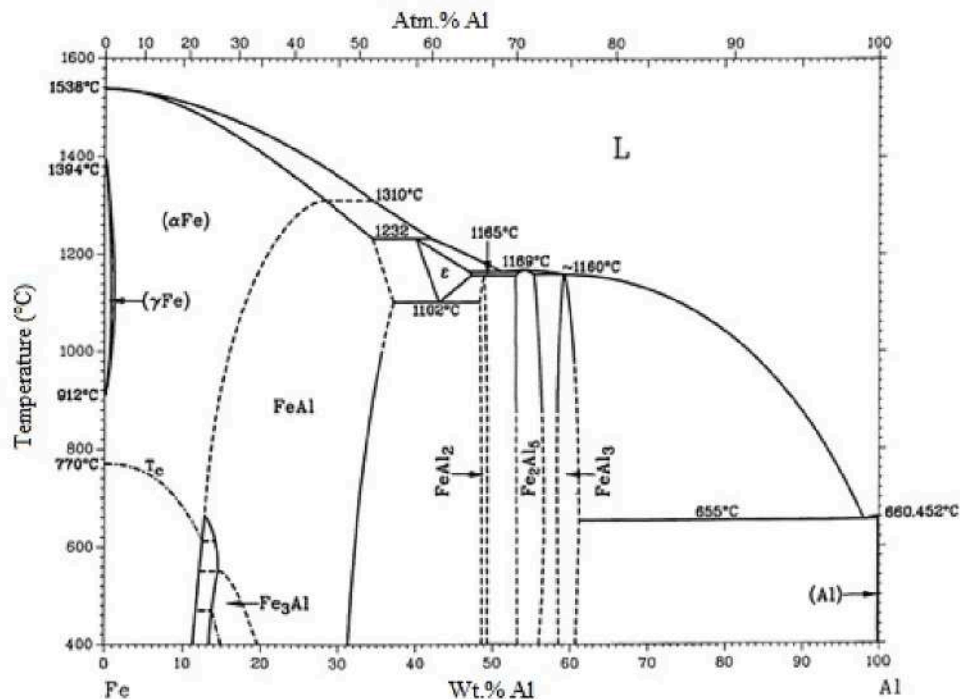


Fig. 4. Fe–Al phase diagram and stability temperatures of  $\text{Fe}_x\text{Al}_y$  phases [60].

aluminide coatings formed on the surface after the aluminizing process on the mechanical properties of the matrix phase in the as-built WAAM ER307 specimen after aluminizing, and the results are presented in Table 1.

As seen in Table 1, the nano-hardness values of the as-built ER307 sample are  $3.15 \pm 0.27$  GPa, and the elasticity modulus values are  $126.09 \pm 6.43$  GPa. However, after aluminizing, the matrix region's hardness and the elasticity modulus values were determined as  $5.02 \pm 0.36$  GPa and  $130.32 \pm 2.75$  GPa, respectively. It is believed that this circumstance resulted from a heat treatment similar to the spheroidization heat treatment applied at  $700^\circ\text{C}$  for 3 h, improving the material's microstructure (refining structures such as pores and inclusions). On the other hand, the nano-hardness value of the coating layer in alumina was determined to be  $13.22 \pm 0.64$  GPa, and the modulus of elasticity was  $156.50 \pm 3.28$  GPa.

### 3.4. Isothermal oxidation test results

The XRD patterns of as-built WAAM ER307 samples measured after oxidation tests at  $1000^\circ\text{C}$  for 5, 25, and 50 h are given in Fig. 5. The results of SEM and EDS line analyses of the samples exposed to oxidation tests are shown in Fig. 6 (5 h), Fig. 7 (25 h), and Fig. 8 (50 h).

The XRD analysis results of WAAM ER307 alloy specimens exposed to different oxidation periods at  $1000^\circ\text{C}$  provided quite important information. As seen in Fig. 5a, while the XRD pattern of the as-built WAAM ER307 alloy consists of a sharp  $\gamma$ -austenite (FCC) phase, a noticeable decrease in the peak intensity of the  $\gamma$ -austenite structure was observed (especially the 111 plane) after the 5 h oxidation period (Fig. 5b). In addition, it was determined that the dominant phases  $\square$ -Fe<sub>3</sub>O<sub>4</sub> and  $\blacktriangle$ - $\alpha$ -FeCr (BCC) as well as  $\circ$ -Fe<sub>2</sub>O<sub>3</sub> minor phases were also formed together with the  $\gamma$ -austenite phase in the structure (see Fig. 5b). When this is compared with the SEM-EDS line analysis of the 5 h sample in Fig. 6, the oxide layer of the sample in question appears to be around  $\sim 12\ \mu\text{m}$ . When the EDS-line diagram is looked at, the atomic weight percentages of Fe, Cr, and O elements in the oxide layer with a thickness of  $\sim 12\ \mu\text{m}$  are much higher than the other elements. Therefore, it can be said that the phases obtained in the XRD result perfectly agree with the SEM-EDS results. Because the oxide layer thickness is small, the peak of the  $\gamma$ -austenite phase comes from the substrate material or is caused by local breaks in the oxide layer.

After the oxidation period of 25 h, the  $\gamma$ -austenite, Fe<sub>3</sub>O<sub>4</sub>, and Fe<sub>2</sub>O<sub>3</sub> peaks were observed as in the 5 h sample, the Fe<sub>2</sub>O<sub>3</sub> peaks were

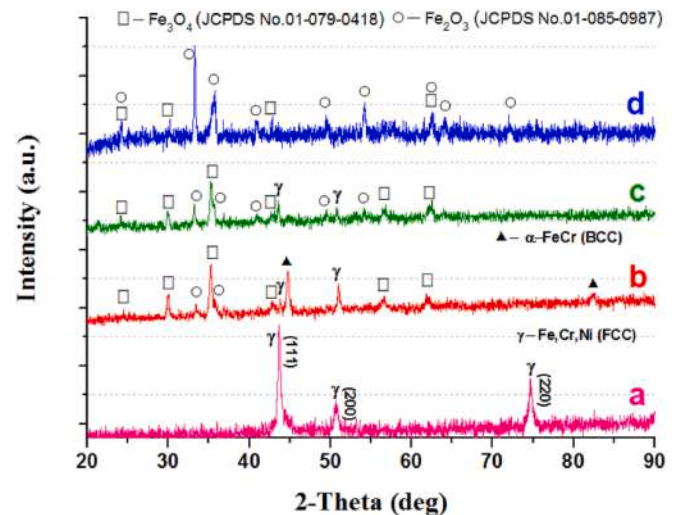


Fig. 5. XRD patterns of WAAM ER307 alloy specimens: a) as-built specimen, and after oxidation tests at  $1000^\circ\text{C}$  for b) 5 h, c) 25 h, and d) 50 h.

observed more clearly, the intensity of  $\gamma$ -austenite peaks decreased and  $\alpha$ -FeCr phases disappeared (Fig. 5c). Moreover, the oxide layer thickness formed on the surface of the WAAM ER307 sample increased to  $\sim 30\ \mu\text{m}$  as a result of the 25-h oxidation period (Fig. 7). When the EDS analysis of the alloy exposed to 25-h oxidation period is examined, it can be seen that the Cr % is greatly reduced (Fig. 7). Therefore, the absence of  $\alpha$ -FeCr phase in Fig. 5c can be associated with the increase in oxidation period and the penetration of % Cr in the structure from the oxide layer on the material surface to the inner regions. On the other hand, in the samples with an oxidation period of 50 h, it is seen that the Fe<sub>2</sub>O<sub>3</sub> peaks become much more dominant compared to Fe<sub>3</sub>O<sub>4</sub>, the  $\gamma$ -austenite phase disappears entirely. Looking at the SEM-EDS line analyses of the 50 h sample (Fig. 8), it was seen that an oxide layer of  $\sim 45\ \mu\text{m}$  was formed on the surface, and the atomic percentages of Fe and O elements were higher than the other elements. Therefore, it is expected that the  $\gamma$ -austenite phase, considered to be the base phase, is not seen in the XRD analysis and that the Fe<sub>2</sub>O<sub>3</sub>, Fe<sub>3</sub>O<sub>4</sub> phases are observed. In addition, it can be seen from the Fe—O phase diagram (Fig. 9) that the Fe<sub>2</sub>O<sub>3</sub> phase is observed when the percentage of oxygen increases [62]. Therefore, this can be associated with the increase in the oxidation time in the EDS analysis, with the atomic percentage of oxygen increasing immediately and the Fe<sub>2</sub>O<sub>3</sub> phase being dominant in the XRD pattern. All the results obtained are fully compatible with SEM-EDS line analyses.

According to the studies in the literature, the X-ray diffraction method is the technique with the highest accuracy among common phase quantification methods (EBSD, ferroscope, etc.) [63]. Therefore, the quantitative phase analysis can be performed with the XRD device using the Debye-Scherrer technique. The average grain (crystallite) size,  $D$ , of the alloys was calculated using the Debye-Scherrer equation [64]:

$$D = \frac{K\lambda}{\beta \cos\theta} \quad (1)$$

where the  $K$  is a constant (0.94),  $\lambda$  is the X-ray wavelength ( $1.5406\ \text{\AA}$  for Cu  $K\alpha$ ),  $\beta$  is the full-width half maximum (FWHM) of the peak relating to  $2\theta$ . In addition to the grain morphology of the alloys, the dislocation density and microstrain parameters are important parameters that determine the microstructure. Dislocations play a significant role in determining the strength and flow properties of metals and alloys. Dislocation density,  $\delta$  is a function of average crystallite size from the XRD pattern;

$$\delta = \frac{1}{D^2} \quad (2)$$

**Table 1**  
Nanoindentation test values of WAAM ER307 stainless steel samples.

Specimen	Nanoindentation testing					
	Indent	$h_c$ (nm)	$h_{max}$ (nm)	$E_r$ (GPa)	$H$ (GPa)	$h_f$ (nm)
Aluminide layer	Indent-1	151.22	200.42	159.82	13.95	109.44
	Indent-2	157.59	207.05	153.27	12.94	116.94
	Indent-3	158.84	207.28	156.41	12.76	117.38
	Indent-1	256.56	293.96	129.17	5.28	224.35
	Indent-2	259.09	294.90	133.46	5.18	228.60
	Aluminized matrix	Indent-3	275.79	310.84	128.33	4.61
As-built WAAM ER307	Indent-1	260.21	299.30	133.10	3.42	229.75
	Indent-2	275.64	315.49	124.73	3.15	237.71
	Indent-3	286.52	321.72	120.45	2.88	253.87

Note:  $h_c$ : contact depth,  $h_{max}$ : maximum depth,  $E_r$ : Reduced elastic modulus,  $H$ : Nano-hardness,  $h_f$ : final displacement.

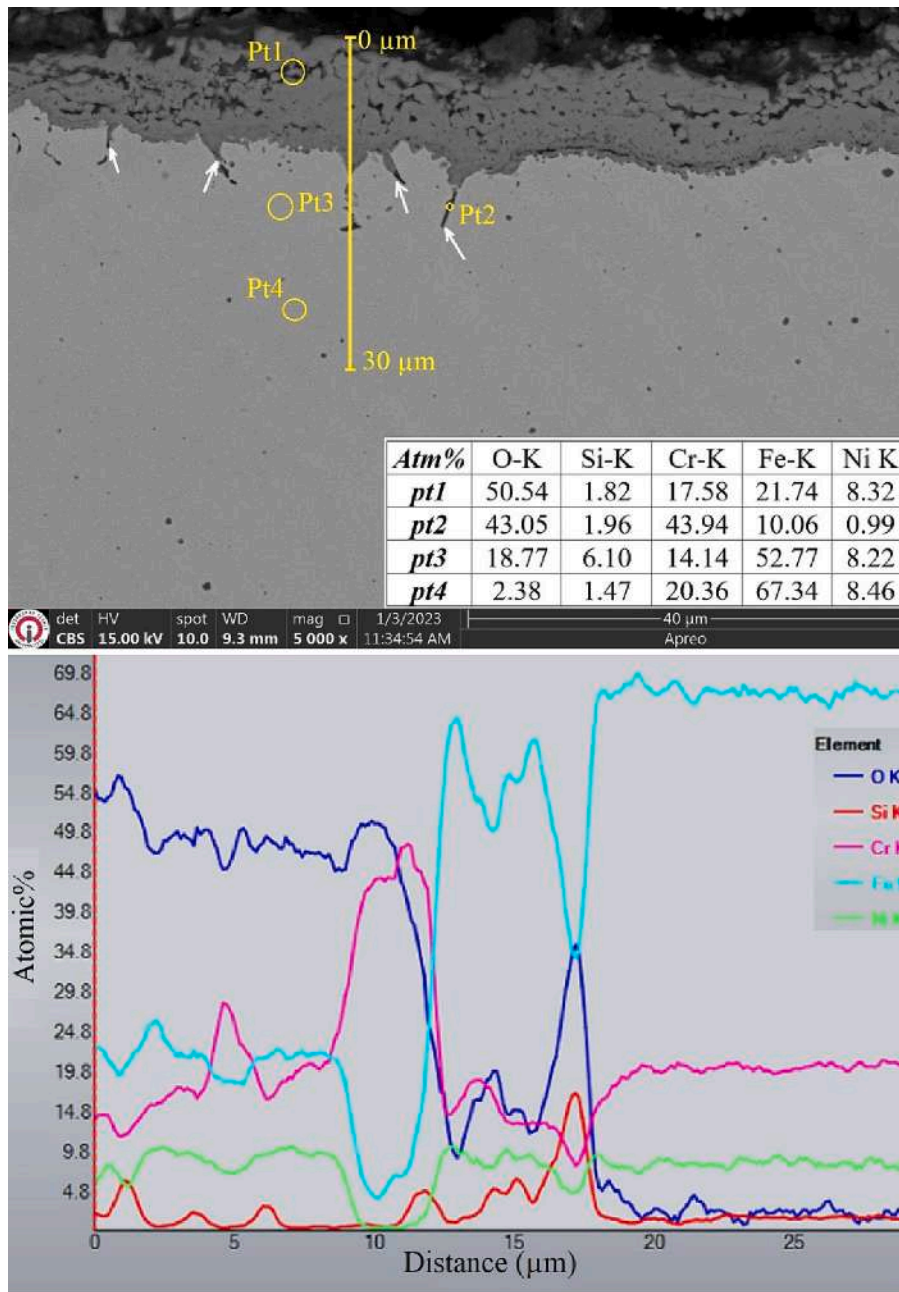


Fig. 6. Cross-sectional SEM view and EDS analysis of the oxide layer grown on the surface of the as-built WAAM ER307 stainless steel component after a 5-h oxidation period.

The degree of distortion in the crystallite lattice of the structure is expressed as microstrain. Both average crystallite size and microstrain in the crystallite lattice affect the line broadening (FWHM) in the X-ray diffraction pattern. Therefore, determining the microstrain of the structure is important for the crystallography of alloys of different orientations. The microstrain,  $\epsilon$  is given in the following Eq. 3;

$$\epsilon = \frac{\beta}{4\tan\theta} \tag{3}$$

In Table 2, the average crystallite size, dislocation density, and the micro tension values of the plane corresponding to the dominant peak of each phase obtained as a result of XRD measurements conducted on the as-built sample and the specimens exposed to oxidation test for 5 h, 25 h, and 50 h.

When Table 2 is examined, as the oxidation time for the  $\gamma$ -austenite

phase increases, a partial increase is observed in the microstrain value, which is the degree of deterioration in the crystal lattice or crystal defect. As the oxidation time increased, the crystal lattice structure of the  $\gamma$ -austenite phase deteriorated, causing the crystal structure to change and disappear completely (see XRD pattern of the specimen exposed to oxidation test for 50 h in Fig. 5d). It was observed that as the oxidation time increased, the average crystallite size of the  $\text{Fe}_2\text{O}_3$  and  $\text{Fe}_3\text{O}_4$  phases decreased and the residual stress values increased accordingly. The decrease in crystallite size may be due to the oxidation process applied at high temperatures above the recrystallization temperature. Normally, it would be expected that grain growth and a decrease in the dislocation density would occur when a material is held at high temperatures for a long time. The stresses in oxidation are caused by thermal expansion differences and the stresses arising from this difference during cooling. This situation can be explained by the fact that

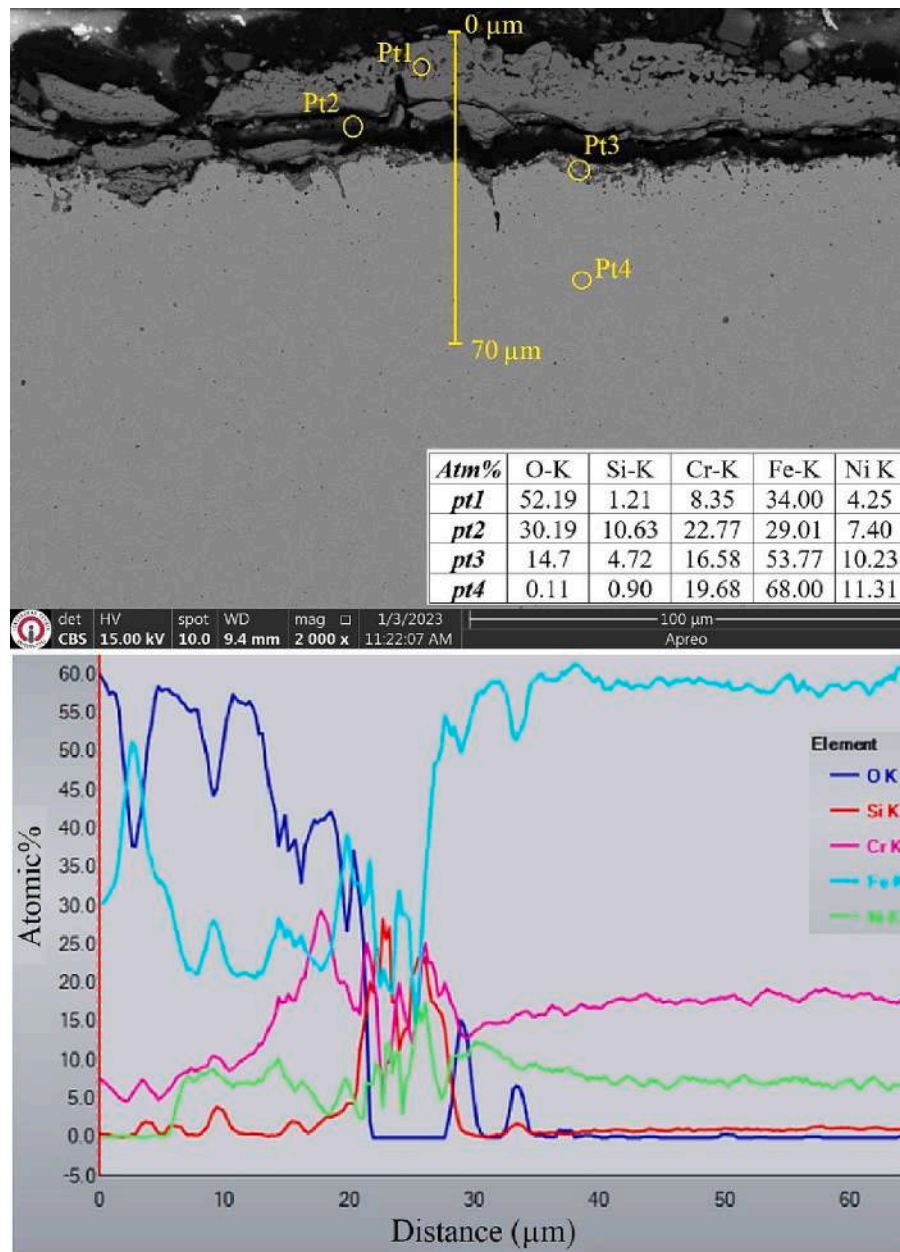


Fig. 7. Cross-sectional SEM view and EDS analysis of the oxide layer grown on the surface of the as-built WAAM ER307 stainless steel component after a 25-h oxidation period.

the oxide layer does not expand sufficiently upon heating and has to contract too much while cooling. However, depending on the increase in oxidation time, it is seen that the microstrain values of the  $\text{Fe}_3\text{O}_4$  phase decreased at 25 h oxidation period whereas it increased at 50 h oxidation period. This result can be explained by the FWHM values related to the grain distortion, dislocation density and residual stresses on the surface of the materials [65]. In the XRD pattern, the FWHM value of the dominant peak ( $35.23^\circ$ ) in the (311) plane of the  $\text{Fe}_3\text{O}_4$  phase was 0.41 in 5 h, 0.38 in 25 h and the peak completely disappeared in 50 h. Therefore, the decrease in the FWHM value at 25 h, that is, the narrowing of the diffraction peak, causes the defects in the structure to decrease and the microstrain values to reduce. As the oxidation time increased to 50 h, a defect occurred in the crystal lattice and the  $\text{Fe}_3\text{O}_4$  phase began to decompose. In addition, the microstrain values of the  $\text{Fe}_2\text{O}_3$  phase decreased due to the increase in the oxidation period. In conclusion, the microstrain values of the  $\text{Fe}_2\text{O}_3$  phase depended on the increase in the oxidation time, an improvement was observed in the

crystal lattice structure of the  $\text{Fe}_2\text{O}_3$  phase, while the crystal lattice structure deteriorated in the  $\text{Fe}_3\text{O}_4$  phase.

The oxide layers formed on the cross-sectional surfaces of untreated as-built and aluminized WAAM ER307 stainless steel specimens after the oxidation test were characterized, and the cross-sectional surfaces of the samples were examined with SEM to support the XRD (Fig. 5) results. EDS analyses were recorded (Figs. 6-8).

When the SEM cross-section micrograph of the oxide layer grown on the surface of the as-built WAAM sample after a 5-h oxidation period is examined (Fig. 6), it was determined that the Pt1 region (the region where cracks are present), where the formed oxide layer is around  $\sim 12 \mu\text{m}$ , contained 50.54 % O, 17.85 % Cr, 21.74 % Fe, and 8.32 % Ni (in atomic %). These findings indicated that this region consists of complex oxide layers (i.e., chromium and iron oxides), as indicated in XRD analysis. Moreover, these results align with Benafia et al.'s findings [66]. In the Pt2 region, the structure (the toothed structure formed towards the interior) is composed mainly of Cr and O. This situation, as Stott and

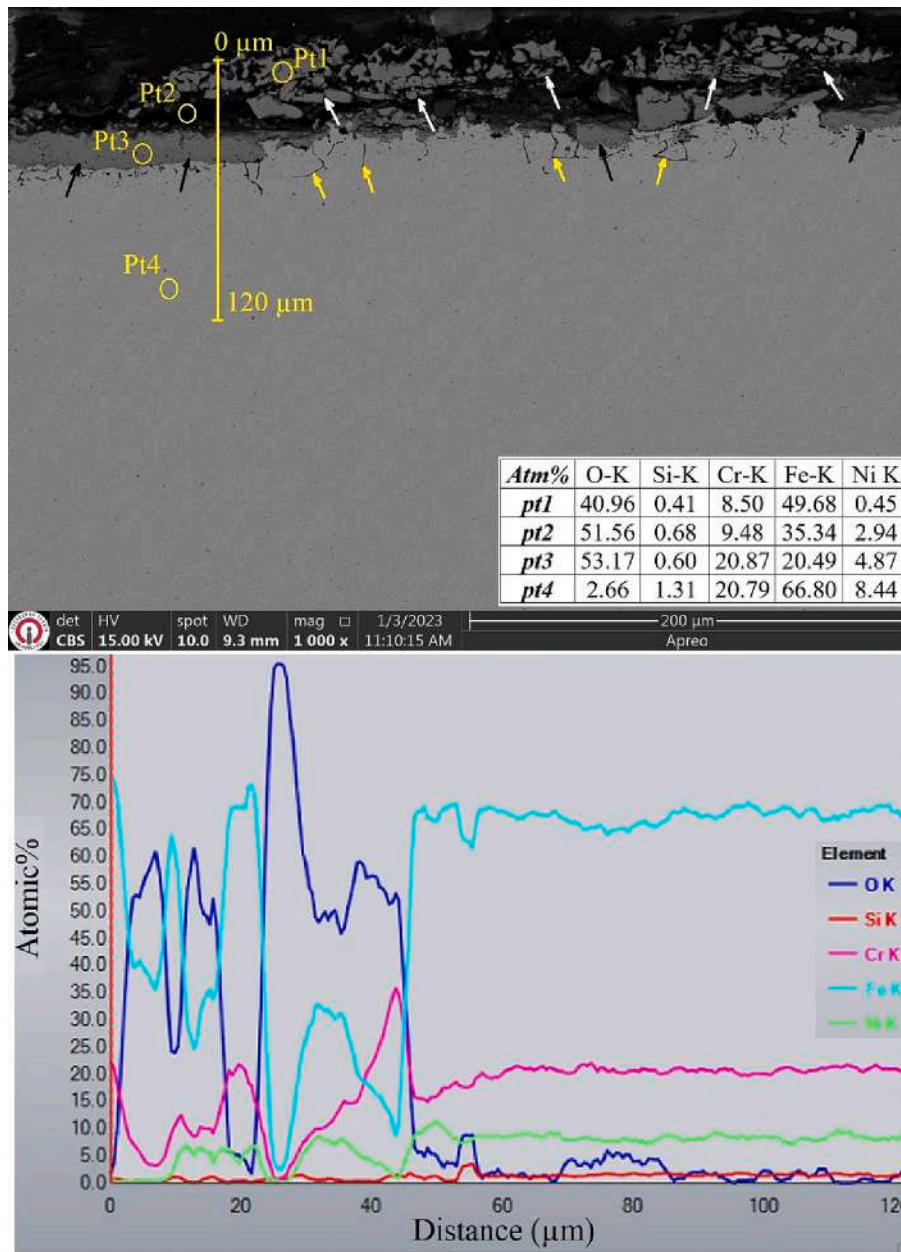


Fig. 8. Cross-sectional SEM view and EDS analysis of the oxide layer grown on the surface of the as-built WAAM ER307 stainless steel component after a 50-h oxidation period.

Wei stated, indicates that Cr<sub>2</sub>O<sub>3</sub> forms at the early stages of the oxidation due to the sufficient chromium content in stainless steels. Furthermore, in the later stages, depending on the duration of oxide growth, blisters of a certain scale form and, upon their contact with Fe, allow oxygen penetration into steel, in which chromium is completely depleted [67]. The remarkable point in the Pt3 region is the accumulation of Si content. It is understood from the EDS results that the Pt4 region is the matrix region.

In the as-built WAAM sample, which was exposed to a 25 h oxidation treatment (Fig. 7), a thicker oxide layer was formed than in the 5 h oxidized sample. However, it was determined that a crack was formed between the oxide layer and the substrate, and the amount of Cr and Ni in the Pt1 region was relatively low compared to the 5 h sample. In contrast, there was an increase in the amount of Fe in this region. These results show that with increasing oxidation time, the Cr<sub>2</sub>O<sub>3</sub> oxide layer turns into a volatile CrO<sub>3</sub> phase, disappears, and is replaced by Fe<sub>2</sub>O<sub>3</sub> and Fe<sub>3</sub>O<sub>4</sub> phases, as determined in XRD analyses. Furthermore, the fact

that Cr increased from the surface to the inner part of the oxide layer, as detected in the EDS line analysis, supports this claim.

When the SEM cross-sectional micrograph of the oxide layer grown on the surface of the as-built WAAM ER307 sample, for which the oxidation time was applied as 50 h, was examined (Fig. 8), it was observed that although the oxide layer was broken off, it was thicker (i. e., 45 µm) than 25 h oxidized sample. There was significant breakage and fall-off on most of the surface. It is seen that the oxide layer content was mainly composed of Fe and O (Pt1 and Pt2) near the surface, as in the 25 h oxidized sample, while the inner parts consist of an oxide layer containing Fe, O, Cr, Ni elements (Pt3). The Pt4 region, on the other hand, exhibited a composition close to the substrate alloy's content, which clearly showed that this part is not affected by oxidation exposure. The XRD patterns of the 50 h oxidized sample showed that Fe<sub>2</sub>O<sub>3</sub>, Fe<sub>3</sub>O<sub>4</sub>, and spinel (Fe<sub>0.6</sub>Cr<sub>0.4</sub>)<sub>2</sub>O<sub>3</sub> phases were dominant in this sample. However, the Fe<sub>2</sub>O<sub>3</sub> and Fe<sub>3</sub>O<sub>4</sub> layers have a higher thermal expansion coefficient than the substrate, while the spinel phases are brittle.

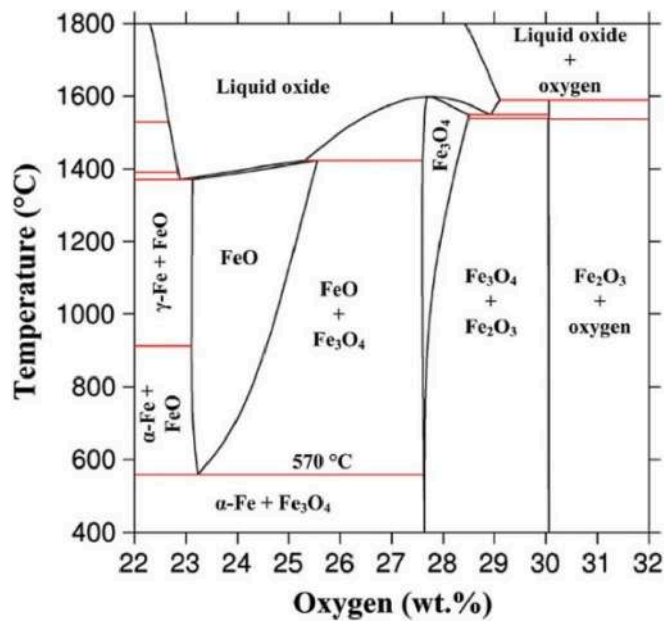


Fig. 9. Iron-oxygen binary equilibrium diagram [62].

Table 2

Dependence of average crystallite size,  $D$ , dislocation density,  $\delta$ , and microstrain,  $\epsilon$ , values of the WAAM ER307 sample on oxidation duration.

Sample name	Phases	$D$ (nm)	$\delta$ (nm) <sup>-2</sup> × 10 <sup>-3</sup>	$\epsilon$
As-built	γ-austenite	25.6	1.53	0.20
5 h	γ-austenite	24.2	1.71	0.21
	Fe <sub>3</sub> O <sub>4</sub>	25.5	1.54	0.29
25 h	γ-austenite	23.6	1.79	0.22
	Fe <sub>2</sub> O <sub>3</sub>	23.5	1.81	0.28
	Fe <sub>3</sub> O <sub>4</sub>	23.8	1.77	0.25
50 h	Fe <sub>2</sub> O <sub>3</sub>	20.2	2.45	0.17
	Fe <sub>3</sub> O <sub>4</sub>	14.9	4.50	0.40

Therefore, they are undesirable due to the higher probability of fragmentation [68].

The XRD patterns of the aluminized WAAM ER307 samples exposed

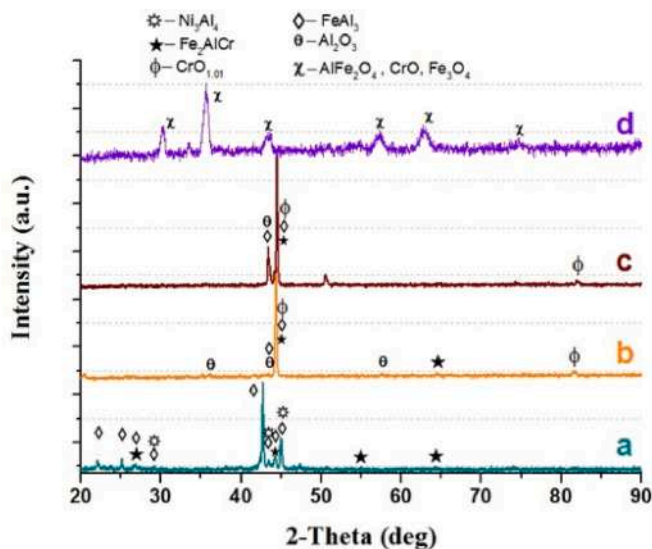


Fig. 10. XRD patterns of as-aluminized WAAM ER307 specimens: a) as-aluminized specimen and as-aluminized samples exposed to oxidation tests at 1000 °C for b) 5 h, c) 25 h and d) 50 h.

to oxidation tests at 1000 °C for 5 h, 25 h, and 50 h are given in Fig. 10, and SEM cross-sectional micrographs and EDS results are shown in Figs. 11-13.

As seen in Fig. 10, dominant phase FeAl<sub>3</sub> is present, as well as minor phases (i.e., Fe<sub>2</sub>AlCr and Ni<sub>3</sub>Al<sub>4</sub> phases) in the aluminide layer formed on the surface of the as-aluminized WAAM ER307 specimen (Fig. 10a), and this was discussed in detail in Section 3.1.

After the 5 h oxidation process, it was determined that Al<sub>2</sub>O<sub>3</sub> and CrO<sub>1.01</sub> phases were formed in the as-aluminized WAAM sample structure. The FeAl<sub>3</sub> and Fe<sub>2</sub>AlCr phases preserved their structure with dominant peaks (Fig. 10b). It was mainly observed that Ni<sub>3</sub>Al<sub>4</sub> phases disappeared due to the formation of Al<sub>2</sub>O<sub>3</sub>. There was a noticeable increase in the peak intensity of the plane corresponding to the FeAl<sub>3</sub> and Fe<sub>2</sub>AlCr phases at ~44.47°. In the 25 h oxidation period, it was determined that the peak of the plane in question, which corresponds to the CrO<sub>1.01</sub>, FeAl<sub>3</sub>, and Fe<sub>2</sub>AlCr phases in the structure, was more pronounced than the 5 h oxidized sample. There was an approximately 20-fold increase in the peak intensity corresponding to the Al<sub>2</sub>O<sub>3</sub> phase at ~43.33° (Fig. 9c). The formation of the CrO<sub>1.01</sub> phase in the structure can be explained by the SEM-EDS line analysis results given in Fig. 11, namely, as it is moved from the material's surface towards the interior, the Cr concentration in atomic % increases and becomes evident in the structure. As seen in the XRD patterns of the 50 h oxidized sample, on the other hand, it was determined that the crystalline structure was severely damaged, the peaks were formed at wider and lower intensities, the structure was completely changed and turned into CrO, Fe<sub>3</sub>O<sub>4</sub>, and AlFe<sub>2</sub>O<sub>4</sub> phases after the 50 h oxidation test. When the SEM-EDS line analysis results given in Fig. 12 are examined, it has been determined that Fe, Cr, O, and Al elements (in atomic %) are much higher than the others, and these findings are in full agreement with the XRD results.

In Table 3, the average grain (crystallite) size, dislocation density, and the micro tension values of the plane corresponding to the dominant peak of each phase, obtained as a result of XRD measurements taken from the as-aluminized sample and aluminized + oxidized specimens (oxidized for 5 h, 25 h, and 50 h), are given. Interesting results were obtained on WAAM ER307 stainless steel specimens exposed to 5 h, 25 h, and 50 h oxidation tests after aluminizing. Accordingly, although an increase was observed in the for the Al<sub>2</sub>O<sub>3</sub> phase in the 5 h oxidation time, a sudden decrease was detected in the 25 h oxidation time. The most important reason for this is the increase in the average grain size of the phase in question by approximately 3.5 times, thus decreasing the dislocation density. The same is true for the FeAl<sub>3</sub> phase. Therefore, the increase in the oxidation time from 5 h to 25 h for these two phases led to the improvement of the crystal structure and its transformation into a stable structure. For the CrO<sub>1.01</sub> phase, with the increase of the oxidation time, the microstrain value decreased, and the average grain size increased. Therefore, the increase in the oxidation time also provided a positive effect on the CrO<sub>1.01</sub> phase. With the increase of the oxidation time from 25 h to 50 h, the crystal lattice structure of the CrO<sub>1.01</sub> phase completely changed and turned into the CrO phase. In addition, depending on the increase in oxidation time, different new oxidized Fe<sub>3</sub>O<sub>4</sub>, and AlFe<sub>2</sub>O<sub>4</sub> phases were formed. Considering the obtained SEM-EDS results, the atomic percentage of oxygen value increased significantly due to the increase in the oxidation period. On the other hand, increasing the oxidation time to 50 h caused the structure to change completely, the phases formed in the 5 h and 25 h oxidation times to disappear and different new phases were formed.

For the detailed analysis of the oxide layers formed in the aluminide layers as a result of the oxidation tests, the samples were examined by SEM, and EDS analyses were performed on some regions. After the 5 h oxidation period (Fig. 11), it was observed that the aluminide layer evolved from a single layer structure in the as-aluminized state into 4 different microstructure appearances. These regions are: (i) the Pt1 region, where the Al<sub>2</sub>O<sub>3</sub> phase forms as a thin line (~10 μm), (ii) the region where Kirkendall voids (marked by black arrows in Fig. 11) are visible in the aluminide coating layer, (iii) the Kirkendall voids within

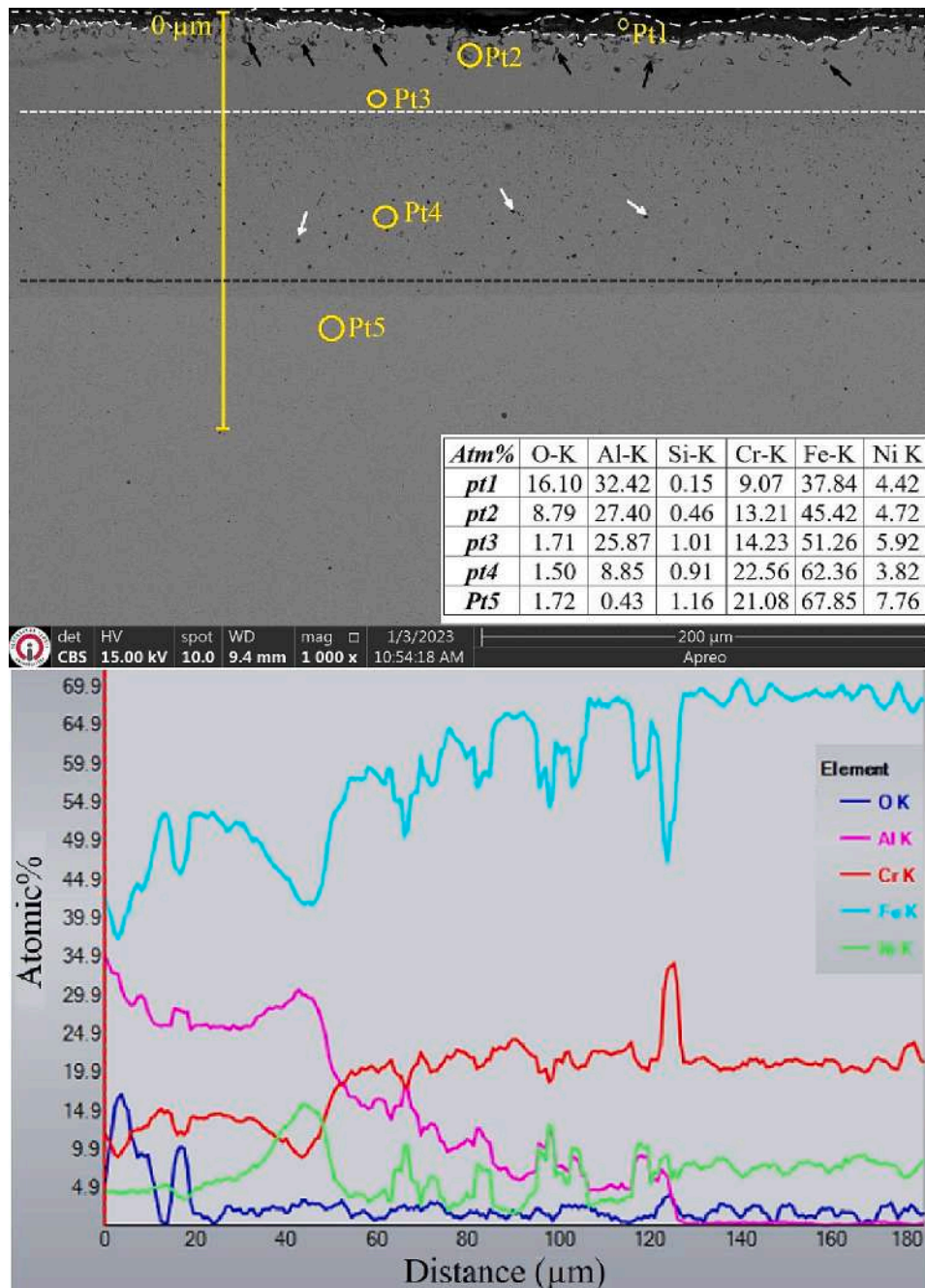


**Fig. 11.** Cross-sectional SEM view and EDS analysis of the oxide layer grown on the surface of the aluminized WAAM ER307 stainless steel component after a 5-h oxidation test.

the aluminide coating layer which appear as dots (marked by white arrows in Fig. 11), and (iv) the substrate material region. Another remarkable point is that the aluminide coating layer, which is 40 μm and contains 60–65 % Al throughout the coating layer after the aluminizing process, increased up to 120 μm thickness at the end of the 5 h oxidation period. The Al ratio gradually decreased from 35.0 % to 0 % from the surface to the inner parts.

In the SEM picture of the Al-25 h oxidized sample (Fig. 12), it is seen that the formation of a 4-layered region is also observed in this sample, as is the case in the Al-5 h oxidized sample. However, it was observed that a large part of the thin Al<sub>2</sub>O<sub>3</sub> layer on the surface was fallen off. This can be explained as follows: the excessive growth of Kirkendall cavities, which are called Region II, took place and consequently led to the fall off of the coating layer on the surface. Increased oxidation time not only

made the Kirkendall formations in Region III more prominent (marked by black arrows in Fig. 12) but also caused the aluminide coating layer to expand from 120 μm to 170 μm compared to the 5 h oxidized sample. The fact that the decrease of the Al ratio to below 10 % at the end of the 25 h oxidation period, which was in the range of 60–65 % (atomic) on the surface after the aluminizing process, and the Al ratio of the aluminide coatings being close to stable throughout the coating unlike the 5 h oxidized sample, indicate that the aluminum diffusion is close to stopping after a certain stage. Wen et al. [69] reported that the formation of Kirkendall cavities begins at the interface between the coating and the matrix, with the aluminide layer becoming more indistinct (unclear) and more irregular with increasing particles and micro-voids developing due to the oxidation of the Al on the surface as a result of increasing oxidation exposure. They explained this irregularity in the

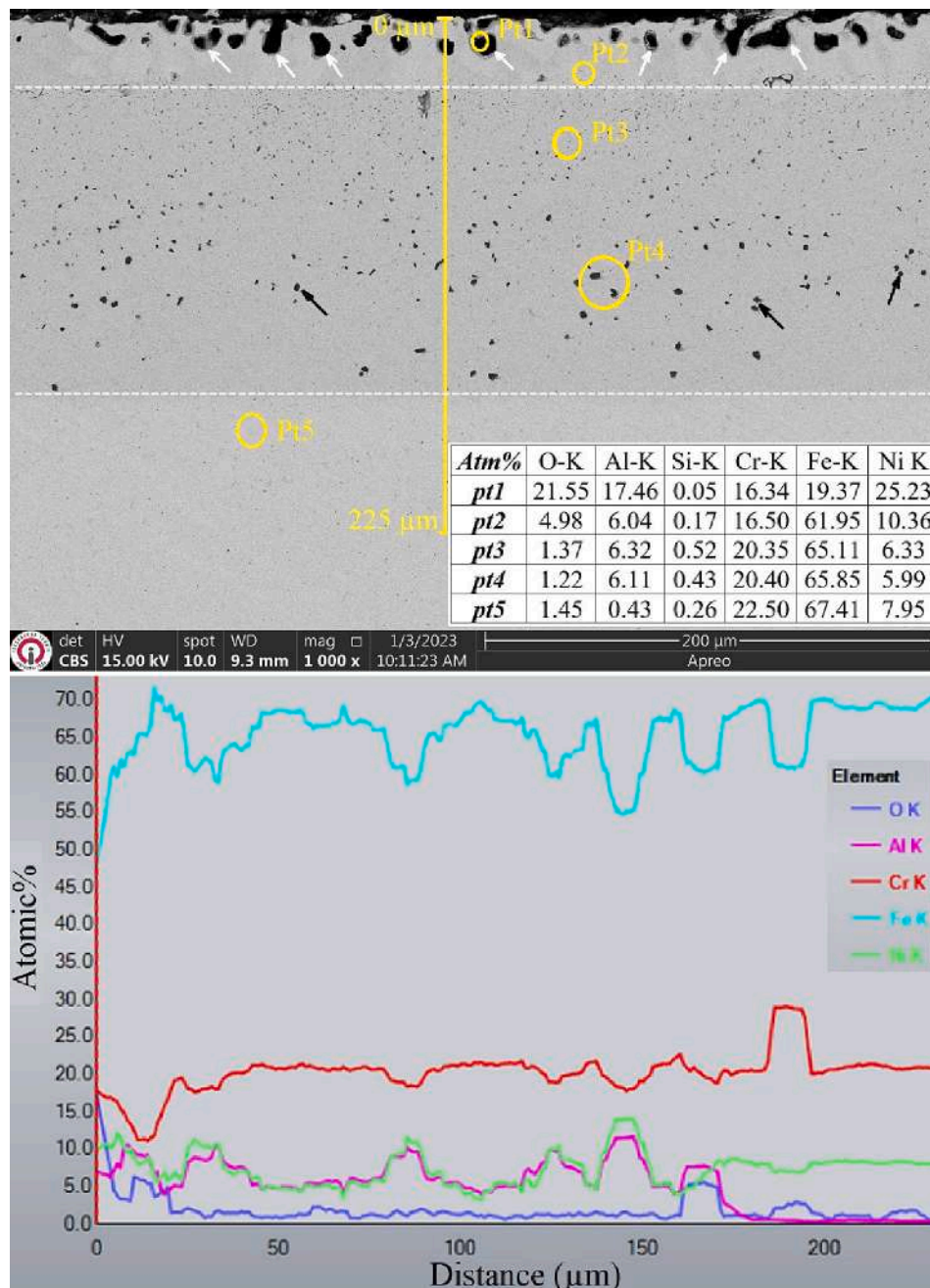


Fig. 12. Cross-sectional SEM view and EDS analysis of the oxide layer grown on the surface of the aluminized WAAM ER307 stainless steel component after a 25-h oxidation test.

structure as the precipitation of increasing carbides in a certain region or accumulation as bulk carbides and the formation of needle-like  $\sigma$  phases as a result.

When the SEM image of the 50 h oxidized sample after aluminizing is examined (Fig. 13), it is seen that the 4-layered region observed in the 5 h and 25 h oxidized samples did not form in this sample, the Kirkendall voids, which were evident in the 25 h oxidized sample, decreased in size. Instead, local  $\text{Cr}_2\text{O}_3$  formations were observed in the top layer. In addition, smaller Kirkendall formations were observed to occur in the lower layer almost throughout the alumina coating layer. Therefore, it was concluded that the large-sized Kirkendall voids seen in the 25 h oxidized sample were not observed in the 50 h oxidized sample due to the fragmentation of the large-void structures due to exposure to increased oxidation time. Because long-term oxidation at high temperatures consumes some of the Al on the surface and causes some of it to

diffuse towards the interior and other may be evaporated. Significantly decreasing Al at the surface creates an Al-depleted region under the scaling (surface oxide layer) interface. The void formation will be facilitated by the irregular internal diffusion of Al, Fe, Cr, and Ni; because elements in aluminide phases rich in Ni, Cr, and Fe diffuse faster than Al [70,71]. Kobayashi et al. [72] reported similar findings in the high-temperature diffusion of carbon steel immersed in a hot pure aluminum bath. The authors determined that void formation caused an increase in the oxidized surface area of the aluminide layer exposed to the oxidation atmosphere, which in turn increased the oxidation rate of the coatings. It has been reported in many studies that the thermal expansion difference between these irregular voids in the oxide layer and the substrate may cause high stresses in the structure, causing oxide fragmentation on the surface. This is in agreement with the weight gain results given in Fig. 14.

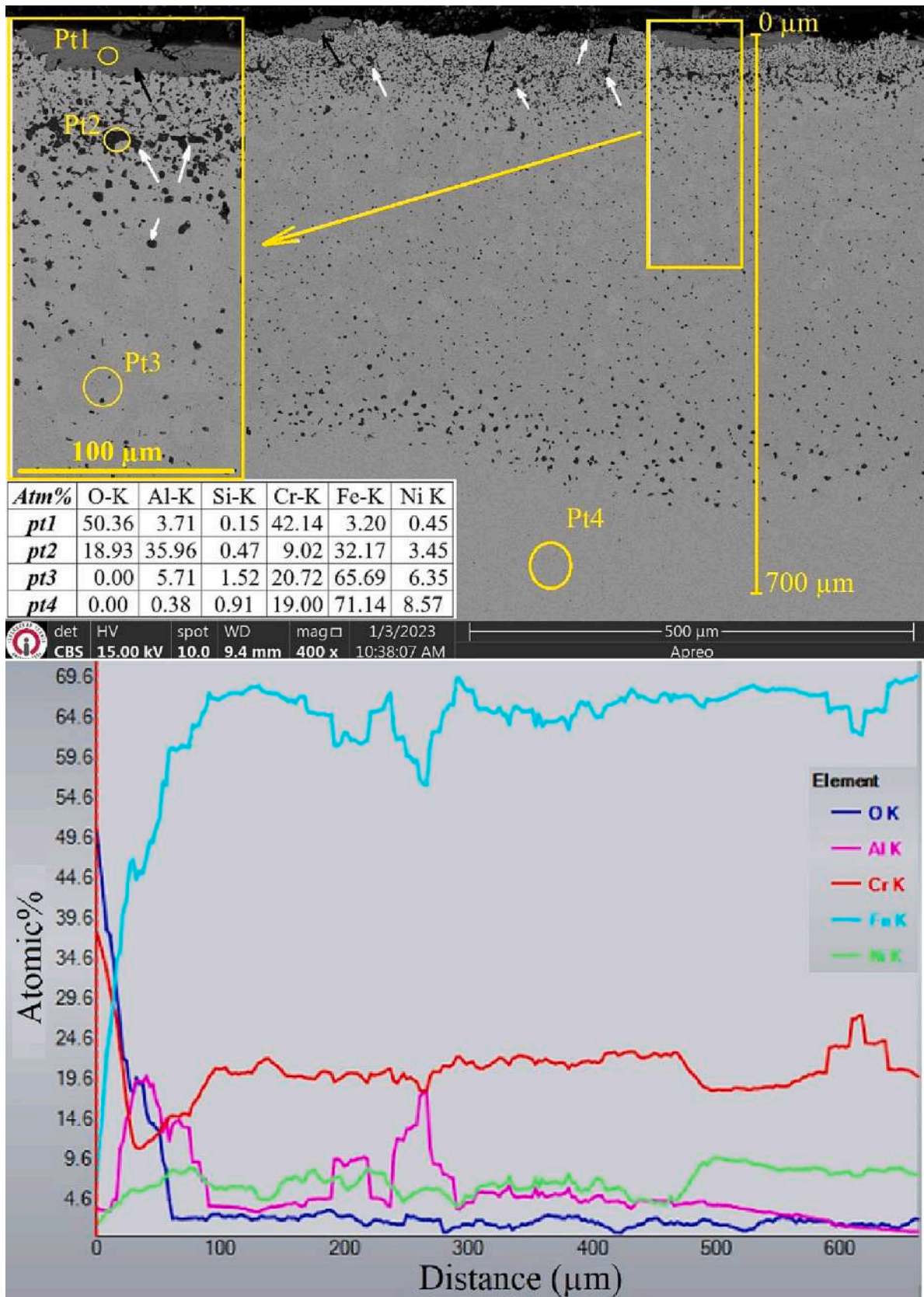


Fig. 13. Cross-sectional SEM view and EDS analysis of the oxide layer grown on the surface of the aluminized WAAM ER307 stainless steel component after a 50-h oxidation test.

**Table 3**

Dependence of average crystallite size,  $D$ , dislocation density,  $\delta$ , and microstrain,  $\epsilon$ , values of the as-aluminized WAAM ER307 sample and samples oxidized for 5 h, 25 h, and 50 h after aluminizing on oxidation duration.

Sample name	Phases	$D$ (nm)	$\delta$ (nm) <sup>-2</sup> × 10 <sup>-3</sup>	$\epsilon$
As-aluminized	Al <sub>2</sub> O <sub>3</sub>	30.50	1.07	0.18
	FeAl <sub>3</sub>	37.79	0.70	0.18
5 h	Al <sub>2</sub> O <sub>3</sub>	23.6	1.79	0.22
	FeAl <sub>3</sub>	24.63	1.65	0.22
	CrO <sub>1.01</sub>	46.47	0.46	0.10
25 h	Al <sub>2</sub> O <sub>3</sub>	74.6	0.17	0.09
	FeAl <sub>3</sub>	61.68	0.26	0.08
	CrO <sub>1.01</sub>	58.75	0.28	0.07
50 h	CrO Fe <sub>3</sub> Al <sub>4</sub> AlFe <sub>2</sub> O <sub>4</sub>	~9.91	~10.2	~0.53

As seen in Fig. 14, the aluminizing process enhanced the oxidation resistance of the samples without exception. This is explained by the fact that the dominant Fe—Al and minor Ni—Al, Cr—Al phases formed on the surface can maintain their stability up to temperatures exceeding 1000 °C [60], as indicated in the section where the XRD analysis was discussed, and the Al<sub>2</sub>O<sub>3</sub> layer formed on the surface of the aluminide coating layer is resistant to the high-temperature oxidation [73–76]. Increasing oxidation time did not cause much loss in improving oxidation resistance. In other words, the aluminide coatings exhibited 1.46, 1.7, and 1.60 times lower weight gains than the untreated sample after the oxidation test times of 5 h, 25 h, and 50 h, respectively.

WAAM ER307 stainless steel could not form protective Cr<sub>2</sub>O<sub>3</sub> after oxidation. Because the amount of Cr is low, the oxidation temperature is high and accordingly, protective Cr<sub>2</sub>O<sub>3</sub> formation did not occur due to the formation of volatile CrO<sub>3</sub> phases. Therefore, Fe<sub>3</sub>O<sub>4</sub> and Fe<sub>2</sub>O<sub>3</sub> phases were formed. Iron-based oxides do not provide a good barrier to oxygen penetration as well as well adherence like chromia and alumina. Besides, thermal expansion mismatches between these oxides and the base material, spallation was observed in the oxide layers and as a result, sufficient oxidation resistance was not observed for these temperatures. The aluminide phases formed beneath the surface after the aluminizing process positively affected the oxidation resistance of WAAM ER307. However, since the aluminide phases formed were not stable aluminides, they showed rapid phase transformations depending on the oxidation temperatures. In addition, due to the high temperatures of the regions near the surface, Kirkendall porosities were formed in the

subsurface regions as a result of rapid cation diffusion, and the adherence of oxides was weakened. In addition, spallation from the oxide layers was observed due to the brittleness of the unstable aluminum-rich phases under the surface, and the protective oxide layer could not show continuity. However, the alumina formed during the oxidation tests partially contributed positively to the oxidation resistance. In addition, as a result of long oxidation tests, the oxide layers showed a break-away oxidation trend due to the weakening of the subsurface regions. As a result, no alumina phases were found on the surface as the aluminum-rich phases were rapidly depleted.

#### 4. Conclusions

In this study, a powder-pack aluminizing process was applied to WAAM ER307 stainless steel samples at 700 °C for 3 h to eliminate the inhomogeneity in the microstructure of ER307 stainless steel produced by the WAAM method and to improve their oxidation resistance. In addition, the effect of aluminide coating on the microstructure, some mechanical properties, and oxidation resistance of ER307 stainless steel components fabricated by the WAAM process were investigated. The outcomes can be summed up as follows:

- 1- Aluminizing resulted in a continuous, homogeneous, dense aluminide layer on the surface of WAAM 307 samples, predominantly consisting of the FeAl<sub>3</sub> phase, with minor amounts of Fe<sub>2</sub>AlCr and Ni<sub>3</sub>Al<sub>4</sub> phases.
- 2- The resulting coating layer is a single-layer coating with a thickness of 43 ± 2.5 µm, and there is a transition zone between (2.5–3.5 µm thickness) the coating layer and the matrix. The hardness value of the aluminide coating layer was determined to be 13.22 ± 0.64 GPa, and the modulus of elasticity was 156.50 ± 3.28 GPa.
- 3- In addition to improving the surface hardness, the aluminizing process homogenized the inter-dendritic structures in the substrate, resulting in a microstructure with higher hardness and modulus of elasticity compared to the as-built samples.
- 4- An improvement in oxidation resistance in the range of 46 %–70 % has been achieved compared to the untreated as-built sample because the aluminide phases forming the aluminide coating layer are stable up to temperatures exceeding 1000 °C, and the Al—O oxide layers formed on the surface containing these phases cut off the contact of oxygen with the substrate.

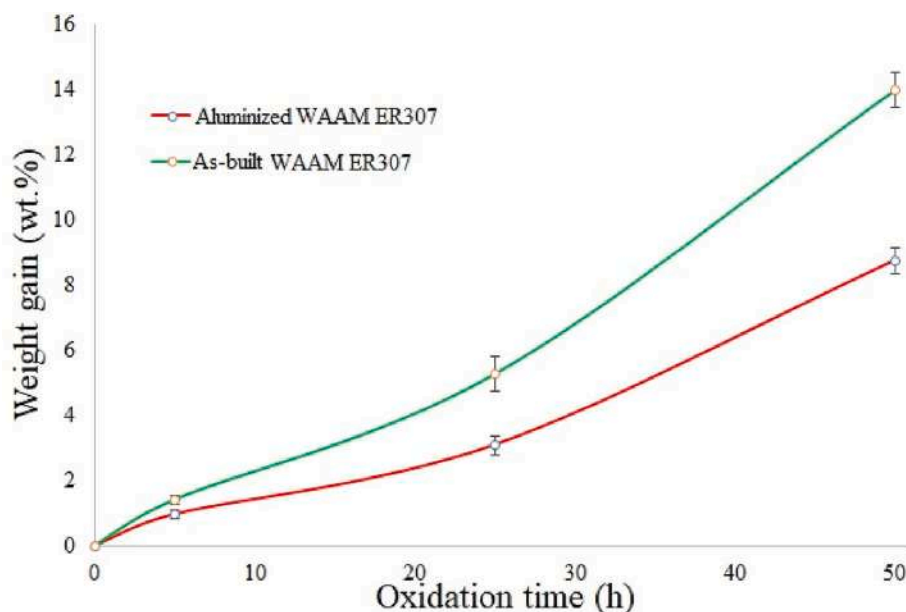


Fig. 14. Variation of weight gains in the as-built and built + aluminized WAAM ER307 specimens with the oxidation test duration.

- 5- While the oxide layer grown on the surface after the 5 h and 25 h oxidation test of the as-built WAAM samples consisted mainly of Fe<sub>3</sub>O<sub>4</sub>, the oxidation test for 50 h resulted in the formation of an oxide layer comprising Fe<sub>2</sub>O<sub>3</sub>.
- 6- Due to the increase in the oxidation time of the As-built WAAM ER307 samples in the oxidation tests, the crystalline properties of the structure increased in the Fe<sub>2</sub>O<sub>3</sub>, while a decrease was observed in the Fe<sub>3</sub>O<sub>4</sub> phase.
- 7- Regarding the micro-strain values, much more different and interesting results were obtained in the aluminized and oxidized WAAM ER 307 samples compared to the as-built and oxidized samples. In this context, the increase in oxidation time from 5 h to 25 h increased the crystallinity. In addition, it improved the structure for Al<sub>2</sub>O<sub>3</sub> and FeAl<sub>3</sub>, and CrO<sub>1.01</sub> phases, regarding the increase in average crystallite size and decrease in dislocation density. On the other hand, increasing the oxidation time to 50 h completely changed the crystal lattice structure and resulted in the formation of new phases, such as CrO, Fe<sub>3</sub>O<sub>4</sub>, and AlFe<sub>2</sub>O<sub>4</sub>.
- 8- Unlike wrought and cast stainless steels, the oxidation of aluminized WAAM ER307 samples was realized in the form of regional Al<sub>2</sub>O<sub>3</sub> formations and Kirkendall voids within aluminide coatings instead of forming a continuous Al<sub>2</sub>O<sub>3</sub> layer on the surface. This can be explained by the fact that the samples produced with WAAM are composed of non-homogeneous regions in the as-built condition. However, this did not cause any adverse effect on oxidation resistance.

This study demonstrated that the applied heat treatment (i.e., aluminizing process) not only minimized the residual stresses and elemental segregation, which is one of the limitations of the WAAM method due to the high-temperature effect but also provided a better matrix in terms of mechanical properties as well as improving the oxidation resistance of stainless steel components produced with WAAM owing to the aluminide coating layer formed on the surface. In addition, the fact that the aluminizing process was performed at a temperature as low as 700 °C has shown that the surface hardness of these alloys can be improved without causing Cr<sub>23</sub>C<sub>6</sub> precipitation and sigma (σ) phase formation, which are significant concerns in heat treatment of stainless steels.

#### CRedit authorship contribution statement

**Uğur Gürol:** Conceptualization, Methodology, Data curation, Writing – review & editing. **Yasemin Altınay:** Data curation, Software, Visualization, Writing – review & editing. **Ali Günen:** Conceptualization, Writing – review & editing, Supervision. **Ömer Saltuk Bölükbaşı:** Conceptualization, Methodology, Writing – review & editing. **Mustafa Koçak:** Conceptualization, Investigation, Writing – review & editing, Supervision. **Gürel Çam:** Conceptualization, Investigation, Writing – review & editing, Supervision.

#### Declaration of competing interest

The authors declare that they have no known competing financial interests or personal relationships that could have appeared to influence the work reported in this paper.

#### Data availability

No data was used for the research described in the article.

#### Acknowledgments

The authors thank Batuhan Turgut and the staff of Gedik Kaynak R&D Center in Istanbul, Turkey for the technical assistance provided during the production of the AISI 307 stainless steel sample using the

WAAM method.

#### References

- [1] J.R. Davis (Ed.), *ASM Speciality Handbook Stainless Steels*, ASM International, Materials Park, Ohio, USA, 1994.
- [2] M. Senol, G. Cam, Investigation into microstructures and properties of AISI 430 ferritic steel butt joints fabricated by GMAW, *Int. J. Press. Vessel. Pip.* 202 (2023), 104926.
- [3] H.T. Serindag, G. Cam, Multi-pass butt welding of thick AISI 316L plates by gas tungsten arc welding: microstructural and mechanical characterization, *Int. J. Press. Vessel. Pip.* 200 (2022), 104842.
- [4] K.H. Lo, C.H. Shek, J.K.L. Lai, Recent developments in stainless steels, *Materials Science and Engineering: R: Reports* 65 (4–6) (2009) 39–104.
- [5] M. Uhrčík, M. Sapieta, Z. Stankovičová, P. Pačcek, M. Oravcová, The stress detection of stainless steel AISI 304, AISI 316L and AISI 316Ti during three-point bending cyclic loading, *Materials Today: Proceedings* 3 (4) (2016) 1189–1194.
- [6] C. Herrera, D. Ponge, D. Raabe, Characterization of the microstructure, crystallographic texture and segregation of an as-cast duplex stainless steel slab, *Steel Research International* 79 (6) (2008) 482–488.
- [7] H. Zhong, R. Wang, Q. Han, M. Fang, H. Yuan, L. Song, Q. Zhai, Solidification structure and central segregation of 6Cr13Mo stainless steel under simulated continuous casting conditions, *Journal of Materials Research and Technology* 20 (2022) 3408–3419.
- [8] P.K. Johnson, Powder metallurgy grows despite challenges, *Advanced materials & processes* 164 (1) (2006) 52–55.
- [9] E. Klar, P.K. Samal, *Powder Metallurgy Stainless Steels: Processing, Microstructures, and Properties*, ASM International, Materials Park, Ohio, USA, 2007.
- [10] H.A. Youssef, *Machining of Stainless Steels and Super Alloys: Traditional and Nontraditional Techniques*, John Wiley & Sons, Hoboken, New Jersey, USA, 2015.
- [11] J.P. Kruth, M.C. Leu, T. Nakagawa, Progress in additive manufacturing and rapid prototyping, *CIRP Ann.* 47 (2) (1998) 525–540.
- [12] T. Wohlers, T. Gornet, History of additive manufacturing, *Wohlers Report* 24 (2014) 118.
- [13] E. Celik, *Additive Manufacturing*, Additive Manufacturing, De Gruyter, Berlin, Germany, 2020.
- [14] R. Singh, J.P. Davim (Eds.), *Additive Manufacturing: Applications and Innovations*, CRC Press, Boca Raton, Florida, USA, 2018.
- [15] R. Duraisamy, S.M. Kumar, A.R. Kannan, N.S. Shanmugam, K. Sankaranarayanan, M.R. Ramesh, Tribological performance of wire arc additive manufactured 347 austenitic stainless steel under unlubricated conditions at elevated temperatures, *J. Manuf. Process.* 56 (2020) 306–321.
- [16] R. Duraisamy, S.M. Kumar, A.R. Kannan, N.S. Shanmugam, K. Sankaranarayanan, Fatigue behavior of austenitic stainless steel 347 fabricated via wire arc additive manufacturing, *J. Mater. Eng. Perform.* 30 (2021) 6844–6850.
- [17] F. Ceritbinmez, A. Gunen, U. Gurol, G. Cam, A comparative study on drillability of Inconel 625 alloy fabricated by wire arc additive manufacturing, *J. Manuf. Process.* 89 (2023) 150–169.
- [18] S. Zhou, H. Xie, J. Ni, G. Yang, L. Qin, X. Guo, Metal transfer behavior during CMT-based wire arc additive manufacturing of Ti-6Al-4V alloy, *J. Manuf. Process.* 82 (2022) 159–173.
- [19] A. Gunen, U. Gurol, M. Kocak, G. Cam, Investigation into the influence of boronizing on the wear behavior of additively manufactured Inconel 625 alloy at elevated temperature, *Progress in Additive Manufacturing* (2023), <https://doi.org/10.1007/s40964-023-00398-8>.
- [20] G. Cam, Prospects of producing aluminum parts by wire arc additive manufacturing (WAAM), *Materials Today: Proceedings* 62 (1) (2022) 77–85.
- [21] S. Cooke, K. Ahmadi, S. Willerth, R. Herring, Metal additive manufacturing: technology, metallurgy and modelling, *J. Manuf. Process.* 57 (2020) 978–1003.
- [22] N. Haghaddi, M. Laleh, M. Moyle, S. Primig, Additive manufacturing of steels: a review of achievements and challenges, *J. Mater. Sci.* 56 (1) (2021) 64–107.
- [23] S. Kokare, J.P. Oliveira, T.G. Santos, R. Godina, Environmental and economic assessment of a steel wall fabricated by wire-based directed energy deposition, *Additive Manufacturing* 61 (2023), 103316.
- [24] M. Ma, Z. Wang, X. Zeng, A comparison on metallurgical behaviors of 316L stainless steel by selective laser melting and laser cladding deposition, *Mater. Sci. Eng. A* 685 (2017) 265–273.
- [25] X. Chen, J. Li, X. Cheng, B. He, H. Wang, Z. Huang, Microstructure and mechanical properties of the austenitic stainless steel 316L fabricated by gas metal arc additive manufacturing, *Mater. Sci. Eng. A* 703 (2017) 567–577.
- [26] W. Jin, C. Zhang, S. Jin, Y. Tian, D. Wellmann, W. Liu, Wire arc additive manufacturing of stainless steels: a review, *Appl. Sci.* 10 (5) (2020) 1563.
- [27] A.R. Kannan, V. Rajkumar, C.D. Prasad, N.S. Shanmugam, J. Yoon, Microstructure and hot corrosion performance of stainless steel 347 produced by wire arc additive manufacturing, *Vacuum* 210 (2023), 111901.
- [28] M.M. Mourad, H.A. Saudi, M.M. Eissa, M.Y. Hassaan, Modified austenitic stainless-steel alloys for shielding nuclear reactors, *Prog. Nucl. Energy* 142 (2021), 104009.
- [29] A.H. Ettefagh, S. Guo, J. Raush, Corrosion performance of additively manufactured stainless steel parts: a review, *Additive Manufacturing* 37 (2021), 101689.
- [30] S. Bruschi, L. Pezzato, A. Ghiotti, M. Dabalà, R. Bertolini, Effectiveness of using low-temperature coolants in machining to enhance durability of AISI 316L stainless steel for reusable biomedical devices, *J. Manuf. Process.* 39 (2019) 295–304.

- [31] P.J. Maziasz, J.T. Busby, Properties of Austenitic Stainless Steels for Nuclear Reactor Applications, Oak Ridge National Lab. (ORNL), Oak Ridge, TN, USA, 2012.
- [32] D.J. Thomas, Advanced active-gas 3D printing of 436 stainless steel for future rocket engine structure manufacture, *J. Manuf. Process.* 74 (2022) 256–265.
- [33] X. Xu, X. Zhang, G. Chen, Z. Lu, Improvement of high-temperature oxidation resistance and strength in alumina-forming austenitic stainless steels, *Mater. Lett.* 65 (21–22) (2011) 3285–3288.
- [34] B.A. Pint, R. Peraldi, P.J. Maziasz, The use of model alloys to develop corrosion-resistant stainless steels, in: *Materials Science Forum* 461, Trans Tech Publications Ltd., 2004, pp. 815–822.
- [35] M. Khenifer, O. Allaoui, M. Taouti, Effect of boronizing on the oxidation resistance of 316L stainless steel, *Acta Phys. Pol. A* 132 (3) (2017) 518–520.
- [36] M. Zandrahimi, J. Vatandoost, H. Ebrahimifar, Pack cementation coatings for high-temperature oxidation resistance of AISI 304 stainless steel, *J. Mater. Eng. Perform.* 21 (2012) 2074–2079.
- [37] J.R. Davis (Ed.), *Surface Hardening of Steels: Understanding the Basics*, ASM International, Materials Park, Ohio, USA, 2002.
- [38] Y. Kayali, E. Kanca, A. Günen, Effect of boronizing on microstructure, high-temperature wear and corrosion behavior of additive manufactured Inconel 718, *Mater. Charact.* 191 (2022), 112155.
- [39] A. Günen, Y. Kanca, İ.H. Karahan, M.S. Karakas, M.S. Gök, E. Kanca, A. Çürük, A comparative study on the effects of different thermochemical coating techniques on corrosion resistance of STKM-13A steel, *Metall. Mater. Trans. A* 49 (11) (2018) 5833–5847.
- [40] D. Wang, Z. Shi, Aluminizing and oxidation treatment of 1Cr18Ni9 stainless steel, *Appl. Surf. Sci.* 227 (1–4) (2004) 255–260.
- [41] S. Rashidi, J.P. Choi, J.W. Stevenson, A. Pandey, R.K. Gupta, Effect of aluminizing on the high-temperature oxidation behavior of an alumina-forming austenitic stainless steel, *JOM* 71 (1) (2019) 109–115.
- [42] E. Öküstözöglü, K.M. Doleker, 904L Paslanmaz Çeliğe Düşük Sıcaklık Alüminyumlamamanın Etkisi, *Avrupa Bilim ve Teknoloji Dergisi* 28 (2021) 1102–1106.
- [43] A. Erdogan, T. Yener, K.M. Doleker, M.E. Korkmaz, M.S. Gök, Low-temperature aluminizing influence on degradation of nimonon 80A surface: microstructure, wear and high temperature oxidation behaviors, *Surfaces and Interfaces* 25 (2021), 101240.
- [44] Z. Zhan, Z. Liu, J. Liu, L. Li, Z. Li, P. Liao, Microstructure and high-temperature corrosion behaviors of aluminide coatings by low-temperature pack aluminizing process, *Appl. Surf. Sci.* 256 (12) (2010) 3874–3879.
- [45] W.C. Oliver, G.M. Pharr, Nanoindentation in materials research: past, present, and future, *MRS Bull.* 35 (11) (2010) 897–907.
- [46] A. Günen, F. Ceritbinmez, K. Patel, M.A. Akhtar, S. Mukherjee, E. Kanca, M. S. Karakas, WEDM machining of MoNbTaTiZr refractory high entropy alloy, *CIRP J. Manuf. Sci. Technol.* 38 (2022) 547–559.
- [47] T.A. Rodrigues, J.D. Escobar, J. Shen, V.R. Duarte, G.G. Ribamar, J.A. Avila, E. Maawad, N. Schell, T.G. Santos, J.P. Oliveira, Effect of heat treatments on 316 stainless steel parts fabricated by wire and arc additive manufacturing: microstructure and synchrotron X-ray diffraction analysis, *Additive Manufacturing* 48 (B) (2021), 102428.
- [48] A. Günen, B. Soyul, Ö. Karakas, Titanium carbide coating to improve surface characteristic, wear and corrosion resistance of spheroidal graphite cast irons, *Surf. Coat. Technol.* 437 (2022), 128280.
- [49] C. Soares, F.E. Mariani, L.C. Casteletti, A.N. Lombardi, G.E. Totten, Characterization of niobium carbide layers produced in ductile cast iron using thermo-reactive treatments, *Mater. Perform. Charact.* 6 (4) (2017) 20160093.
- [50] T. Yener, Low temperature aluminizing of Fe-Cr-Ni super alloy by pack cementation, *Vacuum* 162 (2019) 114–120.
- [51] T. Yener, K.M. Doleker, A. Erdogan, M. Oge, Y. Er, A.C. Karaoglanli, S. Zeytin, Wear and oxidation performances of low temperature aluminized IN600, *Surf. Coat. Technol.* 436 (2022), 128295.
- [52] W. Li, H. Chen, W. Huang, J. Chen, L. Zuo, C. Li, S. Zhang, Effect of laser shock peening on high cycle fatigue properties of aluminized AISI 321 stainless steel, *Int. J. Fatigue* 147 (2021), 106180.
- [53] S.Y. Kim, C.S. Choi, A study on mechanical properties of aluminized steel plate, *Journal of the Korean Institute of Surface Engineering* 13 (2) (1980) 81–86.
- [54] W. Li, H. Chen, C. Li, W. Huang, J. Chen, L. Zuo, S. Zhang, Microstructure and tensile properties of AISI 321 stainless steel with aluminizing and annealing treatment, *Mater. Des.* 205 (2021), 109729.
- [55] Y. Sun, J. Dong, P. Zhao, B. Dou, Formation and phase transformation of aluminide coating prepared by low-temperature aluminizing process, *Surf. Coat. Technol.* 330 (2017) 234–240.
- [56] J. Dong, Y. Sun, F. He, H. Huang, J. Zhen, Effects of substrate surface roughness and aluminizing agent composition on the aluminide coatings by low-temperature pack cementation, *Materials Research Express* 6 (3) (2018), 036409.
- [57] R. Duraisamy, S. Mohan Kumar, A. Rajesh Kannan, N. Siva Shanmugam, K. Sankaranarayanan, Reliability and sustainability of wire arc additive manufactured plates using ER 347 wire-mechanical and metallurgical perspectives, *Proc. Inst. Mech. Eng. C J. Mech. Eng. Sci.* 235 (10) (2021) 1860–1871.
- [58] A. Günen, U. Gürol, M. Koçak, G. Çam, A new approach to improve some properties of wire arc additively manufactured stainless steel components: simultaneous homogenization and boriding, *Surface and Coatings Technology* 460 (129395) (2023) 0257–8972.
- [59] Pranav Praveen Nikam, D. Arun, K. Devendranath Ramkumar, N. Sivashanmugam, Microstructure characterization and tensile properties of CMT-based wire plus arc additive manufactured ER2594, *Materials Characterization* 169 (2020) 1044–5803, <https://doi.org/10.1016/j.matchar.2020.110671>, 110671.
- [60] J.L. Murray, Fe-Al Binary Phase Diagram. Alloy Phase Diagrams, ASM International, Materials Park, Ohio, USA, 1992, p. 54.
- [61] Y. Yang, F. Zhang, J. He, Y. Qin, B. Liu, M. Yang, F. Yin, Microstructure, growth kinetics and mechanical properties of interface layer for roll bonded aluminum-steel clad sheet annealed under argon gas protection, *Vacuum* 151 (2018) 189–196.
- [62] Z.F. Li, Y. Gao, G.M. Cao, Z.Y. Liu, High-efficiency reduction behavior for the oxide scale formed on hot-rolled steel in a mixed atmosphere of hydrogen and argon, *J. Mater. Sci.* 55 (4) (2020) 1826–1839.
- [63] L. Becker, J. Boes, J. Lentz, C. Cui, V. Uhlenwinkel, M. Steinbacher, S. Weber, Quantification of extremely small-structured ferritic-austenitic phase fractions in stainless steels manufactured by laser powder bed fusion, *Materialia* 22 (2022), 101393.
- [64] P. Debye, P. Scherrer, Interference of irregularly oriented particles in x-rays, *Phys. Z.* 17 (1916) 277–283.
- [65] I.C. Noyan, J.B. Cohen, *Residual Stress: Measurement by Diffraction and Interpretation*, Springer, 2013.
- [66] S. Benafia, D. Retrait, S.Y. Brou, B. Panicaud, J.G. Poussard, Influence of surface mechanical attrition treatment on the oxidation behaviour of 316L stainless steel, *Corros. Sci.* 136 (2018) 188–200.
- [67] F.H. Stott, F.I. Wei, High temperature oxidation of commercial austenitic stainless steels, *Mater. Sci. Technol.* 5 (11) (1989) 1140–1147.
- [68] L. Tan, X. Ren, K. Sridharan, T.R. Allen, Effect of shot-peening on the oxidation of alloy 800H exposed to supercritical water and cyclic oxidation, *Corros. Sci.* 50 (7) (2008) 2040–2046.
- [69] J. Wen, C. Fei, S.Y. Ahn, L. Han, B. Huang, Y. Liu, H.S. Kim, Accelerated damage mechanisms of aluminized superalloy turbine blades regarding combined high-and-low cycle fatigue, *Surf. Coat. Technol.* 451 (2022), 129048.
- [70] Y. Zhou, L. Wang, G. Wang, D. Jin, W. Hao, X. Zhao, P. Xiao, Influence of substrate composition on the oxidation performance of nickel aluminide coating prepared by pack cementation, *Corros. Sci.* 110 (2016) 284–295.
- [71] H.J. Grabke, Oxidation of NiAl and FeAl, *Intermetallics* 7 (10) (1999) 1153–1158.
- [72] S. Kobayashi, T. Yakou, Control of intermetallic compound layers at interface between steel and aluminum by diffusion treatment, *Mater. Sci. Eng. A* 338 (1–2) (2002) 44–53.
- [73] K.M. Doleker, The examination of microstructure and thermal oxidation behavior of laser-remelted high-velocity oxygen liquid fuel Fe/Al coating, *J. Mater. Eng. Perform.* 29 (5) (2020) 3220–3232.
- [74] M.C. Galez, C. Oskay, S. Madloch, Microstructural degradation and interdiffusion behavior of NiAl and Ge-modified NiAl coatings deposited on alloy 602 CA, *Surf. Coat. Technol.* 364 (2019) 211–217.
- [75] M. Seifert, G.K. Rane, S.B. Menzel, S. Oswald, T. Gemming, Improving the oxidation resistance of RuAl thin films with Al<sub>2</sub>O<sub>3</sub> or SiO<sub>2</sub> cover layers, *J. Alloys Compd.* 776 (2019) 819–825.
- [76] H. Vasudev, L. Thakur, H. Singh, A. Bansal, An investigation on oxidation behaviour of high velocity oxy-fuel sprayed Inconel718-Al<sub>2</sub>O<sub>3</sub> composite coatings, *Surf. Coat. Technol.* 393 (2020), 125770.